APPLICATION OF A TRANSONIC SIMILARITY RULE TO CORRECT THE EFFECTS OF SIDEWALL BOUNDARY LAYERS IN TWO-DIMENSIONAL TRANSONIC WIND TUNNELS

by

William Grier Sewall

B.S. May 1973, Rensselaer Polytechnic Institute

A Thesis submitted to

The Faculty

of

The School of Engineering and Applied Science

of the George Washington University in

partial satisfaction of the requirements

for the degree of Master of Science

August 1982

APPLICATION OF A TRANSONIC SIMILARITY RULE TO CORRECT THE EFFECTS OF SIDEWALL BOUNDARY LAYERS IN TWO-DIMENSIONAL TRANSONIC WIND TUNNELS

by

William G. Sewall

ABSTRACT

A transonic similarity rule which accounts for the effects of attached sidewall boundary layers is presented and evaluated by comparison with the characteristics of airfoils tested in a two-dimensional transonic tunnel with different sidewall boundary-layer thicknesses. The rule appears valid provided the sidewall boundary layer both remains attached in the vicinity of the model and occupies a small enough fraction of the tunnel width to preserve sufficient two-dimensionality in the tunnel.

ACKNOWLEDGEMENTS

The author wishes to recognize and thank the following individuals for their contributions to this research effort: Dr. Richard W. Barnwell for the original suggestion of the project and for his helpful encouragement; Joel L. Everhart for assistance with the boundary-layer data reduction, suggestion of the means of artificially thickening the sidewall boundary layer, and guidance in the operation of the Langley 6- by 19-Inch Transonic Tunnel; Boyce Lavender and his group of technicians for conscious efforts in carefully conducting the experiment; Jean Foster of LaRC and Sue Davy of SDC for software management efforts; Christine Barnett for her typing services; Dr. Douglas Dwoyer for serving as the thesis advisor; Blair Gloss for his valuable guidance in using the plotting routines; and Betty Millard for her help in figure preparation.

TABLE OF CONTENTS

LIST OF FIGURES

LIST OF SYMBOLS

The units used for the physical quantities in this paper are given in the International System of Units. The measurements and calculations were made in U.S. Customary Units.

b tunnel width, 15.72 cm

C_p static pressure coefficient, $\frac{p_{local} - p_\infty}{q_\infty}$

c airfoil chord, 15.72 cm

c_d section drag coefficient, $\sum_{Wake} c_d' \frac{\Delta y}{c}$

c_d' point drag coefficient,

$$2\left(\frac{p_w}{p_\infty}\right)^{6/7}\left[\frac{\left(\frac{p_{t,w}}{p_w}\right)^{2/7} - 1}{\left(\frac{p_{t,\infty}}{p_\infty}\right)^{2/7} - 1}\right]^{1/2}\left\{\left(\frac{p_{t,w}}{p_{t,\infty}}\right)^{1/7} - \left[\frac{\left(\frac{p_{t,w}}{p_\infty}\right)^{2/7} - 1}{\left(\frac{p_{t,\infty}}{p_\infty}\right)^{2/7} - 1}\right]^{1/2}\right\}$$

c_n section normal-force coefficient.

$$\sum_{\substack{\text{lower}\\ \text{surface}}} C_p \frac{\Delta x}{c} - \sum_{\substack{\text{upper}\\ \text{surface}}} C_p \frac{\Delta x}{c}$$

$\bar{c}_d$ adjusted section drag coefficient

$\bar{c}_n$ adjusted normal-force coefficient

c_p specific heat at constant pressure

c_v specific heat at constant volume

H boundary-layer shape factor, displacement thickness ÷ momentum thickness

$\bar{H}$ transformed shape factor, $\frac{1}{\theta}\int_0^\delta \frac{\rho}{\rho_e}\left(1 - \frac{U}{U_e}\right) dz$

L	effective length of a flat plate having the same boundary layer as a wind-tunnel sidewall
M	local Mach number
M_∞	measured freestream Mach number
$\bar{M}_\infty$	equivalent freestream Mach number
ΔM	difference between the equivalent freestream Mach number and the measured freestream Mach number, $\bar{M}_\infty - M_\infty$
N	exponent for power law used in boundary-layer velocity distribution
P	factor used in the series approximations for the boundary-layer displacement thickness and momentum thickness, $\frac{0.1793\ M_e^2}{1 + 0.1793\ M_e^2}$
$p_{t,w}$	total pressure measured on traversing survey probe and used in the c_d' calculation, kPa
$p_{t,\infty}$	freestream stagnation pressure or total pressure, kPa
p_w	static pressure measured on tunnel sidewall near traversing survey probe and used in the c_d' calculation, kPa
p_∞	freestream static pressure, kPa
q_∞	freestream dynamic pressure, kPa
R	universal gas constant
r	recovery factor used in the temperature distribution equation for the boundary layer, 0.8963
T	local static temperature, ^oK
T_o	stagnation temperature, ^oK
t	maximum thickness-to-chord ratio
U	longitudinal component of velocity
U_∞	freestream velocity

u longitudinal component of perturbation velocity, $u = U - U_\infty$

v vertical component of perturbation velocity

w spanwise component of perturbation velocity

x longitudinal axis, positive in the downstream direction

y vertical axis

z spanwise axis

$\bar{\beta}$ factor in governing equations containing sidewall boundary-layer parameters, $\sqrt{1 - M_\infty^2 + \frac{2\delta^*}{b}\left(2 + \frac{1}{H} - M_\infty^2\right)}$

$\Delta\bar{\beta}$ variable used in the first-order approximation of the sidewall boundary-layer effects, $\frac{2\delta^*}{b}\left(2 + \frac{1}{H} - M_\infty^2\right)$

δ sidewall boundary-layer thickness, cm

δ^* sidewall boundary-layer displacement thickness, cm

$$\int_0^\delta \left(1 - \frac{\rho U}{\rho_e U_e}\right) dz$$

θ sidewall boundary-layer momentum thickness, cm

$$\int_0^\delta \frac{\rho U}{\rho_e U_e}\left(1 - \frac{U}{U_e}\right) dz$$

ρ local static density

τ_w wall shear stress

Subscripts:

e condition at the edge of the boundary layer

1 identifies the first flow field used in the similarity rule

2 identifies the second flow field that is similar to the first flow field used in the similarity rule

Abbreviations:

A.O.A.	angle of attack, degrees
RN	Reynolds number based on the airfoil chord, unless otherwise mentioned
TRANS.	transition from laminar to turbulent boundary layers on airfoil upper and lower surfaces

CHAPTER 1

INTRODUCTION

Since the development of wind tunnels, extensive attention has been devoted to the interference on wind-tunnel models caused by the tunnel wall boundaries. This interference is caused by the alteration of the streamlines near the wall from their free-air positions. Wind-tunnel interference in both two- and three-dimensional facilities has been addressed with analysis and facility modifications to reduce or eliminate it.

In the past, the primary interest in two-dimensional wall interference concerned the upper and lower wall effects. Several of the linear analytical methods that have been developed to account for these effects are presented in reference 1. Some nonlinear methods have also been developed for transonic two-dimensional tunnels and are described in references 2 and 3. Attempts to reduce these interference effects have resulted in facility modifications by making the upper and lower walls with either longitudinal slots, porous surfaces, or adjustable contours.

The interference effects caused by the sidewalls in two-dimensional wind tunnels occur because of the presence of the sidewall boundary layers. The interference of attached sidewall boundary layers in two-dimensional tunnels results in a modification of the continuity equation because the geometric tunnel width

is effectively reduced by twice the sidewall boundary-layer displacement thickness. The two sidewall interference problems which have received the most attention are the growth of the sidewall boundary layer due to the shearing stress at the sidewall and the separation of the sidewall boundary layer due to interaction with large model-induced pressure gradients. The problem of boundary-layer growth due to shearing stress is accounted for in some wind tunnels by a slight outward inclination of the walls, and the problem of the sidewall boundary-layer separation can be concontrolled to some extent with suction or tangential blowing on the sidewall.

This study concerns the intermediate problem of the attached sidewall boundary-layer interaction with the pressure field of the model at transonic speeds. Earlier methods of accounting for this effect have been proposed for incompressible flow, as described in references 4 and 5. These methods considered the effect of the sidewall boundary layer as a change in the circulation about the airfoil.

For subsonic and transonic compressible flow, this effect can be formulated into similarity rules of the sidewall boundary layer to the model-induced pressure field. The analysis presented in this study applies elements of the derivation of the similarity rule given in reference 6 to the von Karman transonic similarity

rule. Experimental results from three airfoil tests, each conducted with varying sidewall boundary-layer thicknesses, are also presented. These results are used to evaluate the validity of the similarity rule at transonic speeds.

CHAPTER 2

EXPERIMENTAL APPARATUS

Facility and Test Conditions

The effects of the sidewall boundary layers in subsonic and transonic two-dimensional tunnels were investigated in the Langley 6- by 19-Inch Transonic Tunnel, presented in figure 1. This facility, described in detail in reference 7, is essentially a blowdown tunnel that operates at Mach numbers ranging from 0.3 to 1.0 with corresponding unit Reynolds numbers of 5.0 million to 7.5 million per foot.

The tunnel axis is oriented vertically with the flow direction upward, as shown in figure 1. The test section has solid, parallel sidewalls and slotted walls joining the sidewalls that minimize the top and bottom wall interference mentioned in reference 1.

This tunnel is configured for testing airfoil models, which span the tunnel, as shown in figure 1, and have constant cross sections consisting of the airfoil shapes. Each end of the model mounts into a turntable that fits flush into the sidewall of the test section. The turntables rotate together, allowing changes in the model angle of attack. A movable rake mounted behind the model is equipped with four total-head tube probes and traverses the wake of the model to obtain wake total pressure measurements used in the drag calculation method from reference 8.

Static pressure measurements both in the test section and in the contraction region 45.7 cm upstream of the start of the test section

are provided by a centerline row of orifices in the surface of one sidewall. On the same sidewall, a turntable with 17 orifices is used to obtain the Mach number at the model station when running tunnel empty for tunnel calibration.

Models

A photograph of two typical models tested in the facility is shown in figure 2. Both models are constructed of stainless steel, have a span of 15.72 cm, and are instrumented for pressure distribution tests. The 15.72-cm chord model, which was the type used in this experiment, has rectangular tangs machined on the ends of the model to transfer the model aerodynamic loads to the model support system. The tubes have been placed inside the model and the coverplate has been welded in place over the tubes. The orifices are located in chordwise rows near the midspan of the model and have a diameter of 0.35 mm. The model contour accuracies for these experiments were within ±0.013 mm.

Three airfoil shapes were used for the experiment. The first model was a NACA 0012 airfoil model, which is a symmetrical airfoil that had been tested in many transonic facilities. The second airfoil to be tested was the supercritical SC-27 airfoil that represented the modern class of transonic airfoils. This particular airfoil has been extensively tested in two neighboring facilities and gave the first indication of an interference problem that was thought to be caused by the sidewall boundary layer. The last model tested was that of the NLR-1 airfoil, another supercritical airfoil that was designed for rotorcraft applications and was tested in a neighboring facility.

All of the airfoil models were tested with a spanwise strip of carborundum grit on both upper and lower surfaces to force the laminar-to-turbulent boundary-layer transition. For the NACA 0012 airfoil, the transition particles were located at 0.075 x/c and were 0.089 mm in nominal height. The SC-27 and NLR-1 airfoil models both had the transition particles located at 0.05 x/c with a nominal particle height of 0.074 mm. The particle sizes were determined by reference 9 so as to insure sufficient size for complete transition without contributing extra protuberance drag.

Artificial Thickening of the Sidewall Boundary Layer

The sidewall boundary effects on two-dimensional airfoil testing were studied by examining results of several airfoil tests conducted with successively thickened sidewall boundary layers. The sidewall boundary layers were thickened with a device similar to that investigated in reference 10, which consisted of thin plates, each having three rows of pins protruding from the surface, as shown in figure 3. One plate was mounted on each sidewall in the tunnel contraction region (fig. 1), at a station 114 cm upstream of the model leading edge as indicated in figure 4. The thickness of the sidewall boundary layer was controlled by the distance that the pins protruded from the plate surface. Three pairs of plates were used: the first pair had no pins, the second pair had pins extending out 2.54 cm, and the third pair had pins extending out 3.80 cm. The plates were mounted as far upstream as was conveniently possible to allow the wakes from the individual pins

to be sufficiently mixed so that no peculiar behavior would exist in the sidewall boundary layers close to the model station.

The sidewall boundary layer was surveyed along the test section centerline using total-head fixed rake-tube probes. These probes consisted of two rows of 0.76 mm o.d. tubes and are shown in figure 5. The tubes were positioned to survey out to 5.10 cm from the sidewall surface. The tube closest to the sidewall rested on the sidewall and was used to determine the skin-friction coefficient from the Preston tube calibration in reference 11. The static pressure at the rake-tube probe position on the sidewall was determined from the static pressure measured at the sidewall location nearest to the probe location without the probe inserted. This static pressure was calibrated against the freestream Mach number so that with the probe mounted, the boundary-layer static pressure was determined from the freestream Mach number.

The velocity ratio, U/U_e, was calculated at each tube position on the rake-tube probe for the different sidewall boundary-layer thicknesses. First, the calibrated static pressure was assumed constant through the boundary layer, and with the local total pressure at a particular tube, the local Mach number was calculated. Next, a static temperature distribution through the boundary layer, given by the equation

$$\frac{T}{T_e} = 1 + 0.1793\left[1 - \left(\frac{U}{U_e}\right)\right]^2 \qquad (1)$$

from references 12 and 13, was used to calculate the local speed of sound. The local velocity at each tube location was then determined from both the local Mach number and speed of sound.

After the local velocities through the boundary layer were obtained, the boundary-layer thickness was determined from a least-squares regression using the power law

$$\frac{U}{U_e} = \left(\frac{z}{\delta}\right)^{1/N} \tag{2}$$

With the values of δ and N and the static temperature given by equation (1), integrations were performed to get the displacement thickness, δ^*, and the momentum thickness, θ. Details of these procedures are given in Appendix A.

To examine the similarity of the thickened sidewall boundary layers, the velocity profiles at the model station were compared. Figure 6 shows the results of this comparison where the variation of the local velocity ratio, U/U_e, with the nondimensional height, z/δ^*, appear for all three boundary-layer thickening configurations. These profiles were considered to match quite well.

Another characteristic investigated for the thickened boundary layers concerned the relationships between the velocities in the boundary layer and the wall shear stress. One relationship for turbulent boundary layers in a zero pressure gradient has been established with the law of the wake of reference 14. The correlation of the three artificially-thickened boundary layers with the law of the wake is shown

in figure 7. The correlation is reasonable except for the inner regions of the boundary layers. This is as expected because the law of the wake applies to the outer regions of the boundary layer while the more commonly known law of the wall applies to the inner region. The rake-tube boundary-layer probes used appear to define primarily the outer region of the boundary layers.

From the law of the wake correlation in figure 7 and the similarity of the velocity distributions in figure 6, it is concluded that the three boundary-layer thickening configurations produced turbulent boundary layers similar to those on a smooth flat plate.

The artificially-thickened sidewall boundary layers were also surveyed in the vicinity of the model station, tunnel empty, to find the variation of boundary-layer displacement thickness. Figure 8 shows this variation to be small for all three boundary-layer thickening configurations. This slow growth rate of the sidewall boundary layer is similar to that due to the shearing stress on a long, flat plate.

The value of the shape factor, H, ranged from 1.39 to 1.59 for the three boundary-layer thickening configurations.

CHAPTER 3

ANALYSIS

Primary Concepts

Consider steady, isentropic, small-perturbation flow in a nominally two-dimensional airfoil wind tunnel. Let the Cartesian coordinates in the freestream, normal, and spanwise directions be x, y, and z; and the respective velocity components be U, v, and w, as shown in figure 9. The effective tunnel width is $b-2\delta^*$ where b and δ^* can vary slightly with respect to x and y, and the boundary conditions for the airfoil model and the upper and lower walls are independent of z. It is also assumed that the tunnel is narrow enough for the flow at each sidewall to be strongly influenced by the other sidewall boundary layer. Reference 6 indicates that to the lowest order, the spanwise velocity varies linearly with the spanwise coordinate z as

$$w = -\frac{2Uz}{b}\frac{\partial \delta^*}{\partial x} \tag{3}$$

In wider tunnels the disturbance caused by the sidewall boundary layer decays nonlinearly with distance from the sidewall so that equation (3) is not valid.

The flow in the wind tunnel described above is governed by the small perturbation form of the continuity equation, which can be written as

$$\left(1 - M_\infty^2\right)\frac{\partial u}{\partial x} + \frac{\partial v}{\partial y} + \frac{\partial w}{\partial z} = (\gamma + 1)M_\infty^2 \frac{u}{U}\frac{\partial u}{\partial x} \tag{4}$$

where M_∞ is the freestream Mach number, $u = U - U_\infty$ is the velocity perturbation in the x-direction, and γ is the ratio of specific heats of the gas.

The dynamics of the sidewall boundary layer are modeled with the von Karman momentum integral, which is given in reference 12 and can be written as

$$\frac{\partial \delta^*}{\partial x} = -\frac{\delta^*}{U}(2 + H - M^2)\frac{\partial U}{\partial x} + \frac{\delta^*}{H}\frac{\partial H}{\partial x} + \frac{\tau_w}{\rho U^2} \tag{5}$$

where ρ is the density and δ^*, τ_w, and H are the sidewall displacement thickness, wall shear stress, and shape factor, respectively.

For the present problem, equation (5) can be simplified because the sidewall boundary layers in the test sections of most airfoil wind tunnels can be approximated as flat-plate boundary layers with large equivalent lengths, L, and hence, relatively large Reynolds numbers. The model pressure field is considered to cause a rather localized variation in this large length-scale sidewall boundary layer, and by applying the following order of magnitude analysis, the shear stress term can be neglected from equation (5).

First, the shape factor gradient, $\frac{\partial H}{\partial x}$, can be related to the velocity gradient, $\frac{\partial U}{\partial x}$, by the following expression derived in Appendix B:

$$\frac{\partial H}{\partial x} = \frac{(H + 1)(H - 1)}{U}\frac{\partial U}{\partial x} \tag{6}$$

Therefore, for a flat plate boundary layer without a pressure gradient, both $\partial U/\partial x$ and $\partial H/\partial x$ vanish in equation (5), leaving only the shear stress term, $\tau_w/\rho U^2$, to affect the sidewall boundary-layer growth rate, $\partial\delta^*/\partial x$. The order of magnitude of $\partial\delta^*/\partial x$ in the test section is δ^*/L which should be the same order as $\tau_w/\rho U^2$.

For the sidewall boundary layer with a pressure gradient due to the model, $\frac{\partial U}{\partial x}$ is of the order $\frac{U}{c}$ so that the first two terms in equation (5) are of the order δ^*/c. Because the equivalent length of the sidewall boundary layer, L, is much larger than the model chord length, c, the inequality

$$\frac{\delta^*}{c} >> \frac{\delta^*}{L} \approx \frac{\tau_w}{\rho U^2} \tag{7}$$

applies[†], and the shear stress term, $\tau_w/\rho U^2$, may be neglected from equation (5) as a first approximation. With equation (6), the final form becomes

$$\frac{\partial\delta^*}{\partial x} = \frac{-\delta^*}{U}\left(2 + \frac{1}{H} - M^2\right)\frac{\partial U}{\partial x} \tag{8}$$

With equation (8), equation (3), and the observation that $\frac{\partial U}{\partial x} = \frac{\partial u}{\partial x}$ the derivative

$$\frac{\partial w}{\partial z} = \frac{2\delta^*}{b}\left(2 + \frac{1}{H} - M^2\right)\frac{\partial u}{\partial x} \tag{9}$$

[†]Measurements of skin friction and δ^* showed values of $\tau_w/\rho U^2$ ranging from 0.0010 to 0.0012 and values of δ^*/c ranging from 0.014 to 0.052, which experimentally verified inequality (7).

is obtained. For small disturbance flow, M in equation (9) can be replaced by the freestream Mach number M_∞. Equation (9) can be combined with equation (4) to give

$$\left[1 - M_\infty^2 + \frac{2\delta^*}{b}\left(2 + \frac{1}{H} - M_\infty^2\right)\right]\frac{\partial u}{\partial x} + \frac{\partial v}{\partial y} = (\gamma + 1)M_\infty^2 \frac{u}{U}\frac{\partial u}{\partial x} \tag{10}$$

or

$$\bar{\beta}^2 \frac{\partial u}{\partial x} + \frac{\partial v}{\partial y} = (\gamma + 1)M_\infty^2 \frac{u}{U}\frac{\partial u}{\partial x} \tag{11}$$

where

$$\bar{\beta} = \sqrt{1 - M_\infty^2 + \frac{2\delta^*}{b}\left(2 + \frac{1}{H} - M_\infty^2\right)} \tag{12}$$

For this study, the values of δ^* and H measured at the model station, tunnel empty, are used as constant values in equation (10) so that the von Karman transonic similarity rule, discussed in reference 15, can be applied. This rule relates the pressure coefficients of two flow fields, denoted by $C_{p,1}$ and $C_{p,2}$, as

$$\frac{(\gamma + 1)M_{\infty,1}^2}{\bar{\beta}_1^{\,2}} C_{p,1} = \frac{(\gamma + 1)M_{\infty,2}^2}{\bar{\beta}_2^{\,2}} C_{p,2} \tag{13}$$

where the flow fields satisfy the constraint

$$\frac{\bar{\beta}_1^{\,2}}{\left[t_1(\gamma_1 + 1)M_{\infty,1}^2\right]^{2/3}} = \frac{\bar{\beta}_2^{\,2}}{\left[t_2(\gamma_2 + 1)M_{\infty,2}^2\right]^{2/3}} \tag{14}$$

For the same model and test gas ($t_1 = t_2$, $\gamma_1 = \gamma_2$), equation (14) becomes

$$\frac{\bar{\beta}_1^2}{(M_{\infty,1})^{4/3}} = \frac{\bar{\beta}_2^2}{(M_{\infty,2})^{4/3}} \quad \text{or} \quad \frac{M_{\infty,1}}{\bar{\beta}_1^{3/2}} = \frac{M_{\infty,2}}{\bar{\beta}_2^{3/2}} \tag{15}$$

An interference-free equivalent Mach number $\bar{M}_\infty$ can be defined with equation (15) and the condition $\delta^* = 0$ as

$$\frac{\bar{M}_\infty}{\left(1 - \bar{M}_\infty^2\right)^{3/4}} = \frac{M_\infty}{\bar{\beta}^{3/2}} \tag{16}$$

This equivalent Mach number represents a flow in an ideal two-dimensional tunnel without a sidewall boundary layer which is otherwise the same as the actual two-dimensional tunnel with a sidewall boundary layer. The pressure coefficient can be adjusted from the value in the actual two-dimensional tunnel to the value in the ideal two-dimensional tunnel having a similar flow without a sidewall boundary layer with equation (13) with $\gamma_1 = \gamma_2$ (same test gas). The expression is

$$\bar{C}_p = \frac{\bar{\beta}}{\sqrt{1 - \bar{M}_\infty^2}} C_p \tag{17}$$

where $\bar{C}_p$ is the pressure coefficient in the ideal two-dimensional tunnel. Equation (17) results in the following adjusted airfoil force coefficients formulated by integrating the surface pressures:

adjusted section normal-force coefficient, $\bar{\bar{c}}_n$,

$$\bar{\bar{c}}_n = \frac{\bar{\beta}}{\sqrt{1 - \bar{\bar{M}}_\infty^2}} c_n \tag{18}$$

adjusted section drag coefficient, $\bar{\bar{c}}_d$,

$$\bar{\bar{c}}_d = \frac{\bar{\beta}}{\sqrt{1 - \bar{\bar{M}}_\infty^2}} c_d \tag{19}$$

where c_n and c_d are the measured section normal-force and drag coefficients.

Approximate Mach Number Increment

An approximate expression for the increment $M_\infty - \bar{\bar{M}}_\infty$ can be formulated from a first-order Taylor series expansion of both sides of equation (16). First, $\bar{\bar{M}}_\infty$ and $\bar{\beta}$ are rewritten as,

$$\bar{\bar{M}}_\infty = M_\infty + \Delta M \tag{20}$$

and

$$\bar{\beta} = \sqrt{1 - M_\infty^2 + \Delta\bar{\beta}} \tag{21}$$

where

$$\Delta\bar{\beta} = \frac{2\delta^*}{b}\left(2 + \frac{1}{H} - M_\infty^2\right) \tag{22}$$

and is treated as a single variable. Equation (16) then appears as

$$\frac{M_\infty + \Delta M}{\left[1 - (M_\infty + \Delta M)^2\right]^{3/4}} - \frac{M_\infty}{\left(1 - M^2\right.^{3/4}} \tag{23}$$

where the only variables are ΔM and $\Delta\bar{\beta}$. Both sides are expanded about ΔM and $\Delta\bar{\beta}$ equal to zero. Retention of the first-order terms of both series results in

$$M_\infty + \Delta M\left[\frac{1}{\left(1 - M_\infty^2\right)^{3/4}} + \frac{3}{2}\frac{M_\infty\,\Delta M}{\left(1 - M_\infty^2\right)^{7/4}} + \cdots\right]$$

$$\approx M_\infty\left[\frac{1}{\left(1 - M_\infty^2\right)^{3/4}} - \frac{3}{4}\frac{\Delta\bar{\beta}}{\left(1 - M_\infty^2\right)^{7/4}}\right] \tag{24}$$

The first-order approximation is

$$\Delta M\left[\frac{1}{\left(1 - M_\infty^2\right)^{3/4}} + \frac{3M_\infty^2}{2\left(1 - M_\infty^2\right)^{7/4}}\right] \approx -\frac{3M_\infty\,\Delta\bar{\beta}}{4\left(1 - M_\infty^2\right)^{7/4}} \tag{25}$$

This equation can be solved for ΔM in terms of $\Delta\bar{\beta}$ to give

$$\Delta M \approx -\frac{3M_\infty}{2\left(2 + M_\infty^2\right)}\Delta\bar{\beta} \tag{26}$$

or

$$\Delta M \approx -\frac{3M_\infty\left(2 + \frac{1}{H} - M_\infty^2\right)(\delta^*/b)}{2 + M_\infty^2} \tag{27}$$

For M_∞ ranging between 0.7 and 0.9 and H ranging from 1.4 to 1.6, this increment is approximately

$$\Delta M \approx -\frac{2\delta^*}{b} \tag{28}$$

which represents the fraction of the tunnel width occupied by the two sidewall boundary-layer displacement thicknesses.

CHAPTER 4

EXPERIMENTAL RESULTS

Equivalent Freestream Mach Number

The effectiveness of the sidewall similarity rule has been evaluated by comparing measured airfoil test data obtained at different sidewall boundary-layer displacement thicknesses. First, the equivalent Mach number, $\bar{M}_\infty$, was determined for the three boundary-layer thicknesses with equations (12) and (16). The value of δ^* and H used in equation (12) were measured at the model station, tunnel empty, as suggested by the analysis. Figure 10 shows the variation of $\bar{M}_\infty$ with M_∞ for the three boundary-layer thicknesses and shows an increment between the equivalent Mach number and the measured freestream Mach number of approximately $2\delta^*/b$ as indicated in equation (28).

NASA 0012 and SC-27 Airfoil Tests

Next, the airfoil tests were conducted beginning with the NACA 0012 airfoil. This airfoil has some interesting transonic behavior at zero angle of attack in that the chordwise shock wave location varies almost linearly with freestream Mach number up to values of approximately 0.84. The variations in shock wave location with both M_∞ and $\bar{M}_\infty$ were compared for the three sidewall boundary-layer thicknesses, as shown in figure 11. A significantly improved correlation was obtained when $\bar{M}_\infty$ rather than M_∞ was used.

The data for the first two sidewall boundary-layer thicknesses are shown in figure 11 with centered symbols, while the data for the third,

or thickest, sidewall boundary layer are shown with open symbols. Other observations that will be mentioned later in the paper indicated that the thickest sidewall boundary layer may have introduced excessive three dimensionality that was not addressed by the present analysis. Therefore, the centered symbols denote the data for which the similarity rule can be applied with the most confidence.

The other two transonic characteristics investigated were the variation of normal-force and section drag coefficient with freestream Mach number at a fixed angle of attack. Here, the similarity rule requires the application of equations (18) and (19) to form the values of the adjusted normal-force and section drag coefficients, $\bar{c}_n$ and $\bar{c}_d$. The variations of the measured normal-force and section drag coefficients, c_n and c_d, with the measured freestream Mach number, M_∞, were compared to the variations of the adjusted normal-force and section drag coefficients, $\bar{c}_n$ and $\bar{c}_d$, with the equivalent freestream Mach number, $\bar{M}_\infty$, for the three sidewall boundary-layer thicknesses.

Continuing with the NACA 0012 airfoil at zero angle of attack, this phase of the investigation began with the comparison of the variation of the measured drag coefficient, c_d, with M_∞ to the variation of the adjusted drag coefficient, $\bar{c}_d$, with $\bar{M}_\infty$. This adjustment actually applies only to the component of pressure drag in the drag coefficient and does not account for the skin-friction component. Figure 12 shows the comparison between c_d vs. M_∞ and $\bar{c}_d$ vs. $\bar{M}_\infty$ for the three sidewall boundary layers. In figure 12, the similarity rule provides a substantially improved drag correlation in the drag-rise region, but

loses quality below the drag rise. This is probably because the majority of the drag comes from the skin friction below drag rise whereas the adjusted drag coefficient addresses only the pressure drag. The correlation improves as the pressure drag becomes a larger fraction of the total drag, as seen in the drag rise region.

Figure 12 indicates more scatter in the drag data measured with the thickest sidewall boundary layer. This boundary layer was approximately 5.2 cm thick at the model station, tunnel empty, so that the two sidewall boundary layers occupied approximately two-thirds of the tunnel width. This large amount of sidewall boundary layer is thought to cause three-dimensional secondary flows not addressed by the analysis, and could possibly have adverse effects on both the drag measurements with the wake probe and the airfoil surface pressure measurements. Therefore, the data for the thickest sidewall boundary layer are presented with open symbols, while the data for the two thinner sidewall boundary layers, where the similarity rule is more applicable, are presented with centered symbols. This depiction was also used in figure 11 and will follow for all figures presenting measured airfoil data with the three sidewall boundary-layer thicknesses.

The variation of normal-force coefficient with freestream Mach number was first studied using the NACA 0012 airfoil at one degree angle of attack. Again, the similarity rule was evaluated by comparing the variation of the measured normal-force coefficient, c_n, with M_∞ to the variation of the adjusted normal-force coefficient, $\bar{c}_n$, with $\bar{M}_\infty$. Figure 13 shows this comparison. The similarity rule provides a

significantly improved correlation, particularly for the two thinner sidewall boundary layers. The correlation quality diminishes for the thickest sidewall boundary layer, probably because of the previously mentioned problems associated with its large thickness. Some loss in correlation also appears for the two thinner sidewall boundary layers near the maximum normal-force coefficient. This is thought to be caused by interactions between the shock wave on the airfoil upper surface with the sidewall boundary layer.

The variation of section drag coefficient with freestream Mach number was also studied for the NACA 0012 airfoil at one degree angle of attack. Figure 14 provides a comparison of c_d vs. M_∞ and $\bar{\bar{c}}_d$ vs. $\bar{\bar{M}}_\infty$. The results are generally similar to the zero angle-of-attack case for this same airfoil in that the correlation improves in the drag rise region.

The SC-27 supercritical airfoil was used to examine the correlation of the adjusted normal-force coefficient with the equivalent Mach number. This airfoil has a much weaker shock wave than that on the NACA 0012 airfoil at the same normal-force coefficient. This would hopefully alleviate the possible interaction between the airfoil shock wave and the sidewall boundary layer that was suspected for the NACA airfoil.

Figure 15 shows the comparison between c_n vs. M_∞ and $\bar{\bar{c}}_n$ vs. $\bar{\bar{M}}_\infty$ for the SC-27 airfoil at zero angle of attack. The correlation is very good for the first two sidewall boundary layers, but degraded somewhat for the thickest sidewall boundary layer. In comparison with the

NACA 0012 airfoil shown in figure 13, the correlation for the SC-27 airfoil for the two thinnest sidewall boundary layers is improved even with the SC-27 at higher values of adjusted normal-force coefficient.

The correlation of $\bar{\bar{c}}_n$ with $\bar{\bar{M}}_\infty$ was examined for the SC-27 airfoil at higher values of c_n and, therefore, stronger airfoil shock waves. Figure 16 shows the comparison between c_n vs. M_∞ and $\bar{\bar{c}}_n$ vs. $\bar{\bar{M}}_\infty$ for an angle of attack of one degree. While the $\bar{\bar{c}}_n$ vs. $\bar{\bar{M}}_\infty$ correlation is still much better than that for c_n vs. M_∞, the correlation for the two thinnest sidewall boundary layers was of lower quality than that shown in the zero angle-of-attack case in figure 15. Therefore, the shock wave strength on the airfoil appears to limit the performance of the similarity rules.

NLR-1 Airfoil Test Results

The NLR-1 airfoil test provided a study of the correlation of the adjusted normal-force and section drag coefficients with equivalent Mach numbers for several angles of attack. As mentioned in the models' description, the NLR-1 is a supercritical airfoil for rotorcraft applications.

Figure 17 shows the comparison of c_n vs. M_∞ and $\bar{\bar{c}}_n$ vs. $\bar{\bar{M}}_\infty$ for an angle of attack of zero. The correlation for the three sidewall boundary layers is improved using $\bar{\bar{c}}_n$ vs. $\bar{\bar{M}}_\infty$ rather than c_n vs. M_∞, but with different results than those observed for the NACA 0012 and SC-27 airfoil data. The largest values of $\bar{\bar{c}}_n$ for the second sidewall boundary layer exceed those of the first or thinnest sidewall boundary layer.

The reason the second sidewall boundary layer produced a larger maximum value of $\bar{c}_n$ than the first sidewall boundary layer was determined from an examination of the local Mach number distributions. Figure 18(a) shows the local Mach number distributions on the NLR-1 airfoil with the two thinnest sidewall boundary layers. The adjusted normal force coefficients are near their maximum respective values shown in figure 17, and these values occur at essentially the same equivalent freestream Mach number. Except for the lower-surface region near 30 percent chord, the local Mach numbers for the thinner sidewall boundary layer are slightly less than those for the thicker sidewall boundary layer at the same location. This condition is required for matched values of the adjusted pressure coefficient which relate directly to the value of $\bar{c}_n$. The value of $\bar{c}_n$ for the thinner sidewall boundary layer is slightly lower than that of the thicker sidewall boundary layer because the lower-surface local Mach numbers at 30-percent chord for both sidewall boundary layers are practically the same. This causes the adjusted pressure coefficients for the thinner sidewall boundary layer to have a larger negative magnitude than that of the thicker sidewall boundary layer in this lower-surface region, and results in a lower value of $\bar{c}_n$.

Figure 18(b) compares the local Mach number distributions for the same two sidewall boundary layers with a small increase in equivalent freestream Mach number. With the thinner sidewall boundary layer, the local Mach numbers on the lower surface between 20- and 50-percent chord have substantially increased from those seen in figure 18(a) with only a

very small change in the equivalent freestream Mach number (0.850 to 0.864). These local Mach numbers for the thinner sidewall boundary layer are significantly higher than those for the thicker sidewall boundary layer. The corresponding higher negative magnitude of the adjusted pressure coefficients in this lower-surface region produce a much lower value of $\bar{c}_n$ for the thinner sidewall boundary layer. The local Mach numbers for the thicker sidewall boundary layer in this same lower-surface region also have a noticeable increase in values compared to those in figure 18(a). The equivalent freestream Mach number for the thicker sidewall boundary layer has only changed from 0.852 (figure 18(a)) to 0.858 (figure 18(b)). This sensitive development of supersonic flow on the lower surface caused an abrupt loss in normal force with increased equivalent freestream Mach number.

This study included two positive angles of attack shown in figures 21 and 22. The correlations of the normal-force coefficient with freestream Mach number for these angles of attack appear very similar to the results for the NACA 0012 airfoil at one degree angle of attack, as indicated by figure 13. First, the $\bar{c}_n$ vs $\bar{M}_\infty$ provides an unquestionable improvement in correlation over the c_n vs M_∞. Second, the correlation of $\bar{c}_n$ vs $\bar{M}_\infty$ loses quality for the data with the thickest sidewall boundary layer as compared to the two thinner sidewall boundary layers. Third, these two thinner sidewall boundary layers show a slight loss in correlation at the maximum values of $\bar{c}_n$, which is probably due to the presence of strong shock waves on the airfoil interacting with the sidewall boundary layer. These shock waves

contributed largely to the rapid drop in $\bar{c}_n$ that follows the maximum value.

Drag measurements were also obtained for the NLR-1 airfoil. These drag data, which are presented in figures 23 through 26, in many cases indicate very similar correlation behavior to that shown for the NACA 0012 airfoil in figures 12 and 13. The correlation of $\bar{c}_d$ vs $\bar{M}_\infty$ shows no real improvement over c_d vs M_∞ until the drag rise region. Drag measurements involving the thickest sidewall boundary layer often seem to show more scatter than that from the two thinner sidewall boundary layers, again, probably because of the large fraction of the tunnel width occupied by the thickest sidewall boundary layer.

Summary of Airfoil Tests Results

For the airfoil data measured with the three sidewall boundary layers, the similarity rule produced an improved correlation for the variation of the adjusted normal-force and section drag coefficients with the equivalent freestream Mach number as compared to the variation of the measured coefficients with the measured freestream Mach number.

The normal-force coefficients appear to form three distinct zones for each sidewall boundary layer when plotted against the measured freestream Mach number. The adjusted normal-force coefficients appear to have more converged zones for the three sidewall boundary layers when plotted against the equivalent freestream Mach number, but the magnitudes of the adjusted normal-force coefficients do not entirely converge.

The section drag coefficients appear to have two distinct drag rise regions for the two thinnest sidewall boundary layers when plotted against the measured freestream Mach number. The adjusted section drag coefficients show converged drag rise regions when plotted against the equivalent freestream Mach number but show no improvement in the magnitude of the drag coefficient when below drag rise.

An important effect of the similarity rule is that the maximum adjusted normal-force coefficient and the divergence that follows occur at almost the same equivalent freestream Mach numbers for all three sidewall boundary layers. Likewise, the drag rise occurs at almost the same equivalent Mach number for the two thinnest sidewall boundary

layers. The fact that the maximum normal force and drag rise occur at different measured freestream Mach numbers for each of the three sidewall boundary layers but at the same equivalent freestream Mach number demonstrates the correction to the measured freestream Mach number provided by the similarity rule.

CHAPTER 5

CONCLUDING REMARKS

The effects of attached sidewall boundary layers in two-dimensional transonic tunnels have been correlated with a transonic similarity rule. It ha been shown experimentally that the application of this similarity rule to the airfoil test data obtained in the Langley 6- by 19-Inch Transonic Tunnel gives an effective freestream Mach number correction. The experimental data also indicate that the similarity rule provides a substantial correction to the normal-force coefficients and some correction for the section drag coefficients in the drag rise region.

The similarity rule correction applies provided the sidewall boundary layer is small enough to avoid excessive three-dimensional interactions with the model. The similarity rule can be used as long as the sidewall boundary layers have no appreciable separation (due to shock wave/boundary layer interaction or significant trailing-edge separation).

REFERENCES

1. Pindzola, M.; and Lo, C. F.: Boundary Interferences at Subsonic Speeds in Wind Tunnels with Ventilated Walls. AEDC TR-69, May 1969.

2. Kemp, William B., Jr.: Transonic Assessment of Two-Dimensional Wind-Tunnel Wall Interference Using Measured Wall Pressures. NASA CP-2045, pp. 473-496, March 1978.

3. Murman, E. M.: A Correction Method for Transonic Wind-Tunnel Wall Interference. AIAA Paper No. 79-1533, July 1979.

4. Preston, J. H.: The Interference on a Wing Spanning a Closed Tunnel, Arising from the Boundary Layers on the Sidewalls, with Special Reference to the Design of Two-Dimensional Tunnels. N.P.L., Teddington, Middlesex, England, R & M 1924, March 1944.

5. Winter, K. G.; and Smith, J. H. B.: A Comment on the Origin of End-Wall Interference in Wind-Tunnel Tests of Airfoils. RAE Tech Memo AERO 1816, August 1979.

6. Barnwell, R. W.: Similarity Rule for Sidewall Boundary-Layer Effect in Two-Dimensional Wind Tunnels. AIAA Journal, Vol. 18, No. 9, pp. 1149-1151, Sept. 1980.

7. Ladson, C. L.: Description and Calibration of the Langley 6- by 19-Inch Transonic Tunnel. NASA TN D-7182, 1973.

8. Baals, Donald D.; and Mourhess, Mary J.: Numerical Evaluation of the Wake-Survey Equations for Subsonic Flow Including the Effects of Energy Addition. NACA WR-L5, 1945. (Formerly NACA ARR L5H27.)

9. Braslow, Albert L.; and Knox, Eugene C.: Simplified Method for Determination of Critical Height of Distributed Roughness Particles for Boundary-Layer Transition at Mach Numbers from 0 to 5. NACA TN-4363, 1958.

10. Johnson, D. F.; and Mitchell, G. A.: Experimental Investigation of Two Methods for Generating an Artificially Thickened Boundary Layer. NASA TM X-2238, 1971.

11. Allen, J. M.: Evaluation of Compressible-Flow Preston Tube Calibrations. NASA TN D-7190, 1973.

12. White, F. M.: Viscous Fluid Flow. McGraw Hill Book Co., New York, p. 607, 1974.

13. Schlichting, H.: Boundary-Layer Theory. McGraw Hill Book Co., New York, pp. 667-668, 1968.

14. Coles, D.: The Law of the Wake in Turbulent Boundary Layers. Journal of Fluid Mechanics, Vol. 1, 1956, pp. 191-226.

15. Liepmann, H. W.; and Rosko, A.: Elements of Gas Dynamics. John Wiley and Sons, Inc., New York, 1957, pp. 256-258.

16. Green, J. E.: Interactions Between Shock Waves and Turbulent Boundary Layers. Progress in Aeronautical Sciences, Vol. XI, Pergamon Press, New York, 1970.

APPENDIX A

BOUNDARY-LAYER DATA REDUCTION

Temperature Distribution in the Boundary Layer

The velocities within the boundary layer were calculated from the values of local Mach number and speed of sound. The local temperature within the boundary layer was given by equation (1), where the wall temperature was assumed to be the adiabatic temperature indicated in reference 13 as

$$T_{aw} = T_{\infty}\left(1 + r\,\frac{\gamma - 1}{2}\,M_{\infty}^2\right) \tag{A1}$$

For the tunnel-empty sidewall boundary layer it was assumed that $T_{\infty} = T_e$, $M_{\infty} = M_e$, and the recovery factor, r, was given a value of 0.8963, which was also obtained from reference 13. The temperature of the chamber surrounding the test section usually remained within $5^{\circ}K$ of the value for T_{aw} in equation (A1). Due to the rapid operation in blowdown testing, the wall temperature was not expected to change significantly.

The temperature distribution through the boundary layer was obtained from reference 12 as

$$\bar{T} = T_{aw} + (T_{aw} - T_w)\,\frac{U}{U_e} - \frac{rU^2}{2c_p} \tag{A2}$$

where $\bar{T}$ is the time-averaged local temperature at some point within the boundary layer. Since T_{aw} is assumed to be the actual wall temperature, T_w, and $U_e^2 = M_e^2\gamma(c_p - c_v)T_e$, equations (A1) and (A2) can be combined to provide equation (1) in the text,

$$\frac{\bar{T}}{T_e} = 1 + r\,\frac{\gamma - 1}{2}\,M_e^2\left(1 - \frac{U^2}{U_e^2}\right) \tag{A3}$$

or

$$\frac{T}{T_e} = 1 + 0.1793\,M_e^2\left(1 - \frac{U^2}{U_e^2}\right) \tag{A4}$$

where $\bar{T}$ is assumed to be the local static temperature, T.

Displacement Thickness and Momentum Thickness Calculations

The sidewall boundary-layer thickness was determined from the least-squares power-law regression given by equation (2) in the text. This procedure was used because the largest sidewall boundary-layer thickness in the experiment exceeded the highest total head tube on the boundary-layer rake-tube probe. Using the power-law representation of the velocity profile in the boundary layer allowed a simple, closed-form integration for calculating the displacement thickness and the momentum thickness.

The boundary-layer displacement thickness δ^* is defined as

$$\delta^* = \int_0^{\delta}\left(1 - \frac{\rho}{\rho_e}\,\frac{U}{U_e}\right)dz \tag{A5}$$

From the ideal gas relation, $p = \rho RT$, and the assumption of zero normal pressure gradient in the boundary layer, the expression $\frac{\rho}{\rho_e} = \frac{T_e}{T}$ is obtained so that equation (A4) becomes

$$\frac{\rho}{\rho_e} = \frac{1}{1 + 0.1793\, M_e^2\left(1 - \frac{U^2}{U_e^2}\right)} \tag{A6}$$

Using the power-law representation of the velocity profile given in equation (2) and equation (A6), equation (A5) becomes

$$\delta^* = \int_0^\delta \left\{1 - \frac{(z/\delta)^{1/N}}{1 + 0.1793\, M_e^2\left[1 - (z/\delta)^{2/N}\right]}\right\} dz \tag{A7}$$

Note that the second term of the integrand is of the form

$$\frac{(z/\delta)^{1/N}}{1 + 0.1793\, M_e^2}\left[\frac{1}{1 - \frac{0.1793\, M_e^2}{1 + 0.1793\, M_e^2}(z/\delta)^{2/N}}\right] \tag{A8}$$

which can be rewritten as the geometric series

$$\frac{(z/\delta)^{1/N}}{1 + 0.1793\, M_e^2}\left[1 + P(z/\delta)^{2/N} + P^2(z/\delta)^{4/N} + P^3(z/\delta)^{6/N} \ldots\right] \tag{A9}$$

where

$$P = \frac{0.1793\, M_e^2}{1 + 0.1793\, M_e^2} \tag{A10}$$

Placement of the series in expression (A9) into equation (A7) allows a term by term integration which results in the series

$$\delta^* = \delta\left[1 + \frac{1}{1 + 0.1793\ M_e^2}\left(\frac{N}{N+1} + \frac{NP}{N+3} + \frac{NP^2}{N+5} + \ldots\right)\right] \qquad \text{(A11)}$$

or

$$\delta^* = \delta + \frac{\delta}{1 + 0.1793\ M_e^2}\left[\sum_{k=1}^{\infty} \frac{NP^{k-1}}{(2k-1) + N}\right] \qquad \text{(A12)}$$

This series converges rapidly and yields the necessary precision when $k = 5$.

The momentum thickness is defined as

$$\theta = \int_0^{\delta} \frac{\rho}{\rho_e}\frac{U}{U_e}\left(1 - \frac{U}{U_e}\right) dz \qquad \text{(A13)}$$

and is calculated in a manner similar to that used for the displacement thickness. With the power-law representation of the velocity profile and the definition of δ^*, equation (A13) becomes

$$\theta = \delta - \delta^* - \int_0^{\delta} \left\{\frac{(z/\delta)^{2N}}{1 + 0.1793\ M_e^2\left[1 - (z/\delta)^{2/N}\right]}\right\} dz \qquad \text{(A14)}$$

The last term in this equation can also be represented by the geometric series

$$\frac{(z/\delta)^{2/N}}{1 + 0.1793\ M_e^2}\left[1 + P(z/\delta)^{2/N} + P^2(z/\delta)^{4/N} + P^3(z/\delta)^{6/N} \ \ldots\right] \qquad \text{(A15)}$$

where $P = \dfrac{0.1793\ M_e^2}{1 + 0.1793\ M_e^2}$ as in equation (A10). Term by term integration yields

$$\frac{\delta}{1 + 0.1793\ M_e^2}\left[\frac{N}{N+2} + \frac{NP}{N+4} + \frac{NP^2}{N+6} + \frac{NP^3}{N+8} \cdots\right]$$

$$= \frac{\delta}{1 + 0.1793\ M_e^2} \sum_{k=1}^{\infty} \frac{NP^{k-1}}{2k + N} \tag{A16}$$

which results in the final equation

$$\theta = \delta - \delta^* - \frac{\delta}{1 + 0.1793\ M_e^2} \sum_{k=1}^{\infty} \frac{NP^{k-1}}{2k + N} \tag{A17}$$

This summation also required 5 terms for convergence to the necessary precision.

APPENDIX B

THE RELATIONSHIP OF THE VELOCITY GRADIENT TO THE SHAPE FACTOR GRADIENT

The conventional shape factor, H, has a significant dependence on freestream Mach number and, therefore, is often replaced by the transformed shape factor, $\bar{H}$. Reference 16 defines the transformed shape factor as

$$\bar{H} = \frac{1}{\theta}\int_0^{\delta} \frac{\rho}{\rho_e}\left(1 - \frac{U}{U_e}\right) dz \tag{B1}$$

For compressible, turbulent boundary layers with constant total temperature assumed through the boundary layer, reference 16 indicates that H is related to $\bar{H}$ by

$$H = (\bar{H} + 1)\left(1 + \frac{\gamma - 1}{2} M^2\right) - 1 \tag{B2}$$

Reference 16 also shows that for large Reynolds numbers, such as those applicable to tunnel sidewall boundary layers, $\bar{H}$ approaches one.† This simplifies equation (B2) to

$$H = 1 + (\gamma - 1)M^2 \tag{B3}$$

---

†The measured values of $\bar{H}$ ranged from 1.18 to 1.26, but use of these values in the above analysis did not provide any significant difference from using $\bar{H} = 1$.

Use of the simple compressible flow relations with constant total temperature results in the expression,

$$U^2 = \frac{M^2 \gamma R T_o}{1 + \left(\frac{\gamma - 1}{2}\right) M^2} \tag{B4}$$

Differentiation of both sides with respect to x gives

$$2U \frac{\partial U}{\partial x} = \left\{ \frac{2M\gamma R T_o}{1 + \left(\frac{\gamma - 1}{2}\right) M^2} - \frac{M^2 \gamma R T_o (\gamma - 1) M}{\left[1 + \left(\frac{\gamma - 1}{2}\right) M^2\right]^2} \right\} \frac{\partial M}{\partial x} \tag{B5}$$

Division of both sides by $2U^2$ and use of equation (B4) yields

$$\frac{1}{U} \frac{\partial U}{\partial x} = \left\{ \frac{2}{M\left[2 + (\gamma - 1) M^2\right]} \right\} \frac{\partial M}{\partial x} \tag{B6}$$

which relates the velocity gradient to the Mach number gradient.

The shape factor gradient can be related to the Mach number gradient by

$$\frac{\partial H}{\partial x} = 2(\gamma - 1) M \frac{\partial M}{\partial x} \tag{B7}$$

with equation (B3), and the Mach number gradient can be related by the velocity gradient with equation (B6), so that

$$\frac{\partial H}{\partial x} = (\gamma - 1) M^2 \left[2 + (\gamma - 1) M^2\right] \frac{1}{U} \frac{\partial U}{\partial x} \tag{B8}$$

With equation (B3), the expression $(\gamma - 1)M^2 = H - 1$ results, and the final form of equation (6) in the text is obtained as

$$\frac{\partial H}{\partial x} = \frac{(H + 1)(H - 1)}{U} \frac{\partial U}{\partial x} \tag{B9}$$

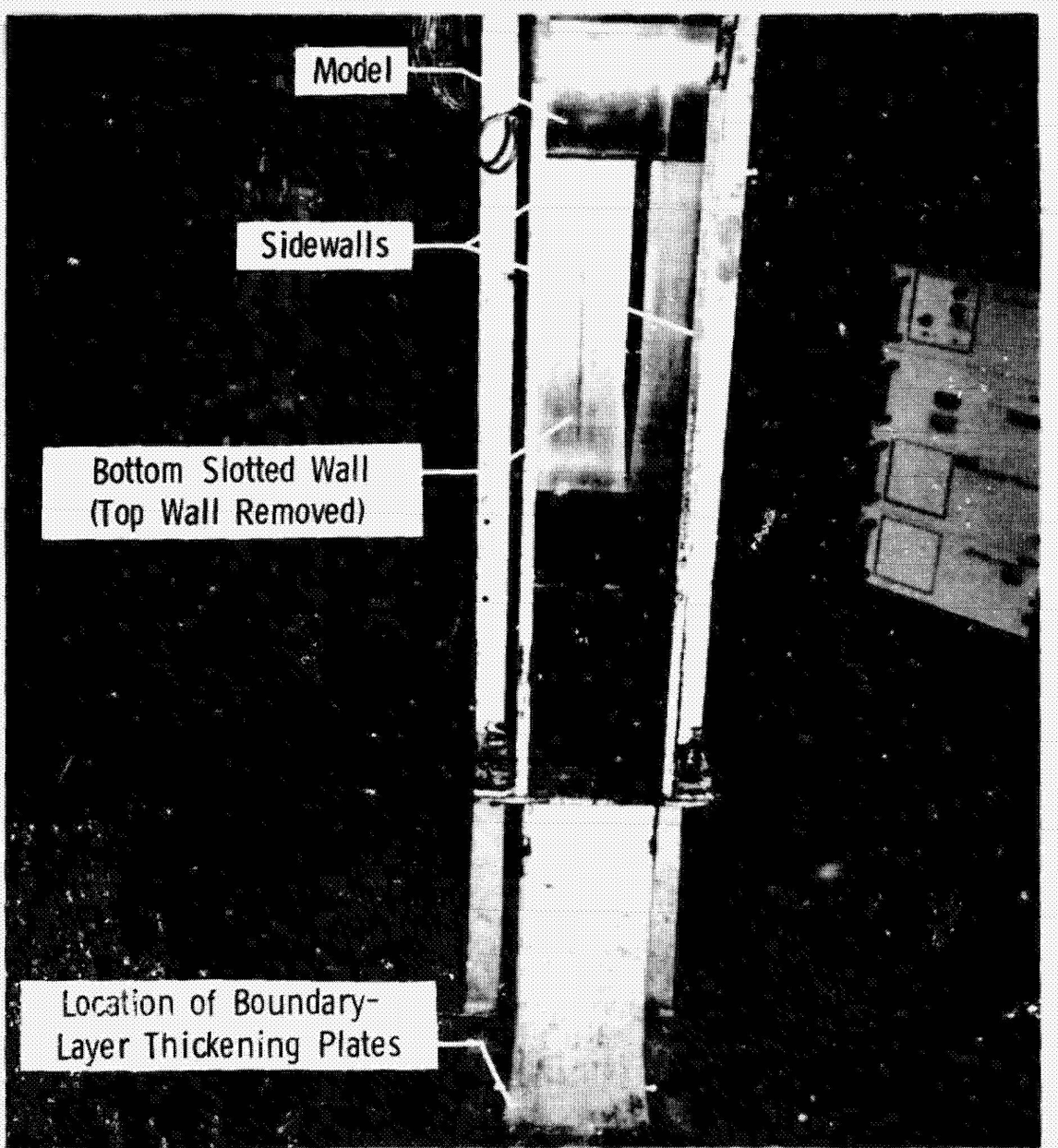

Figure 1.- Photograph of the Langley 6- by 19-Inch Transonic Tunnel showing a top view of the test section.

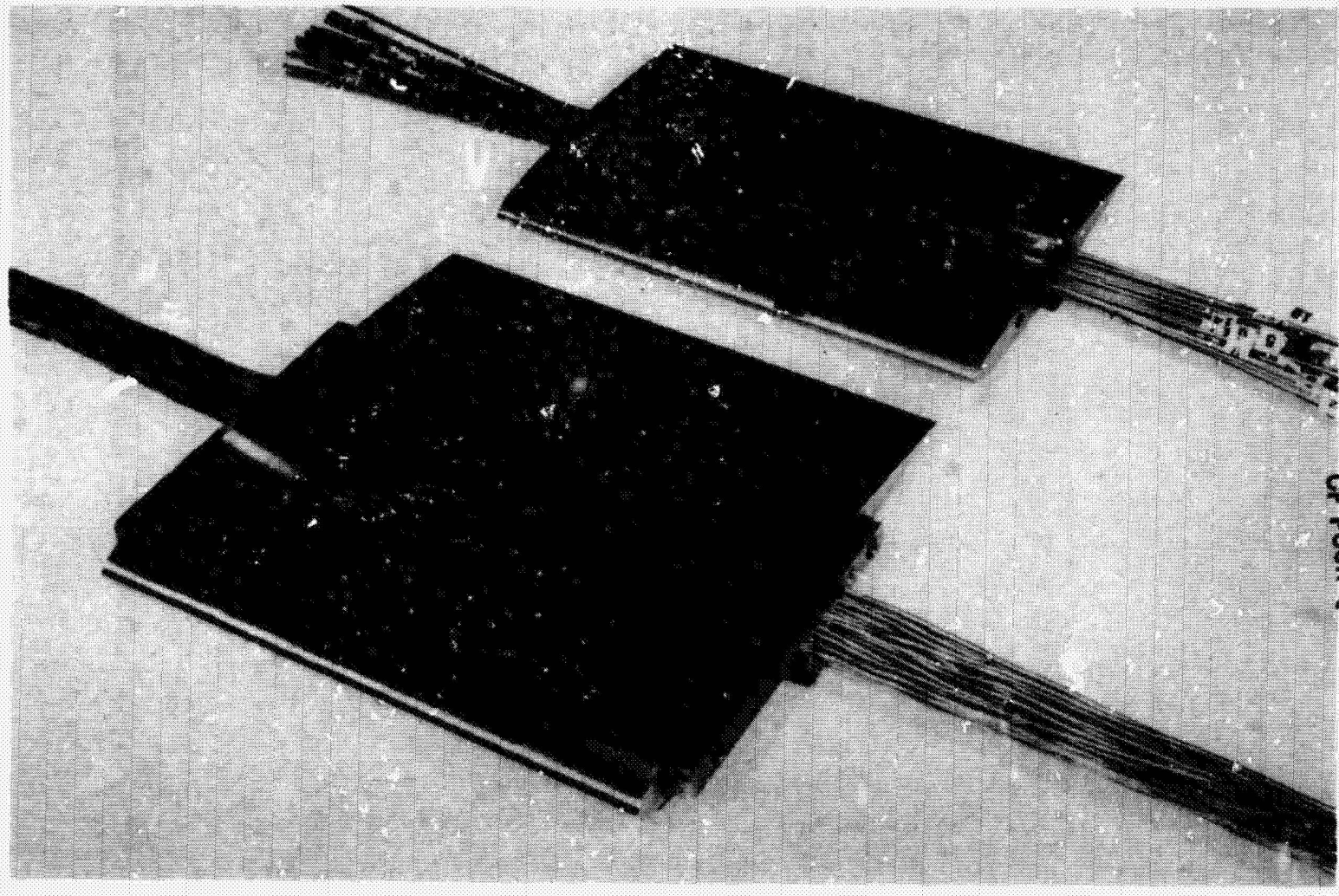

L-75-234

Figure 2.- Photograph of typical models instrumented for pressure tests; 15.24-cm model in foreground and 10.15-cm model in background.

Figure 3.- Photograph of the three artificial boundary-layer thickening configurations showing the plates with pins that are 3.80 cm and 2.54 cm long and a plate without pins.

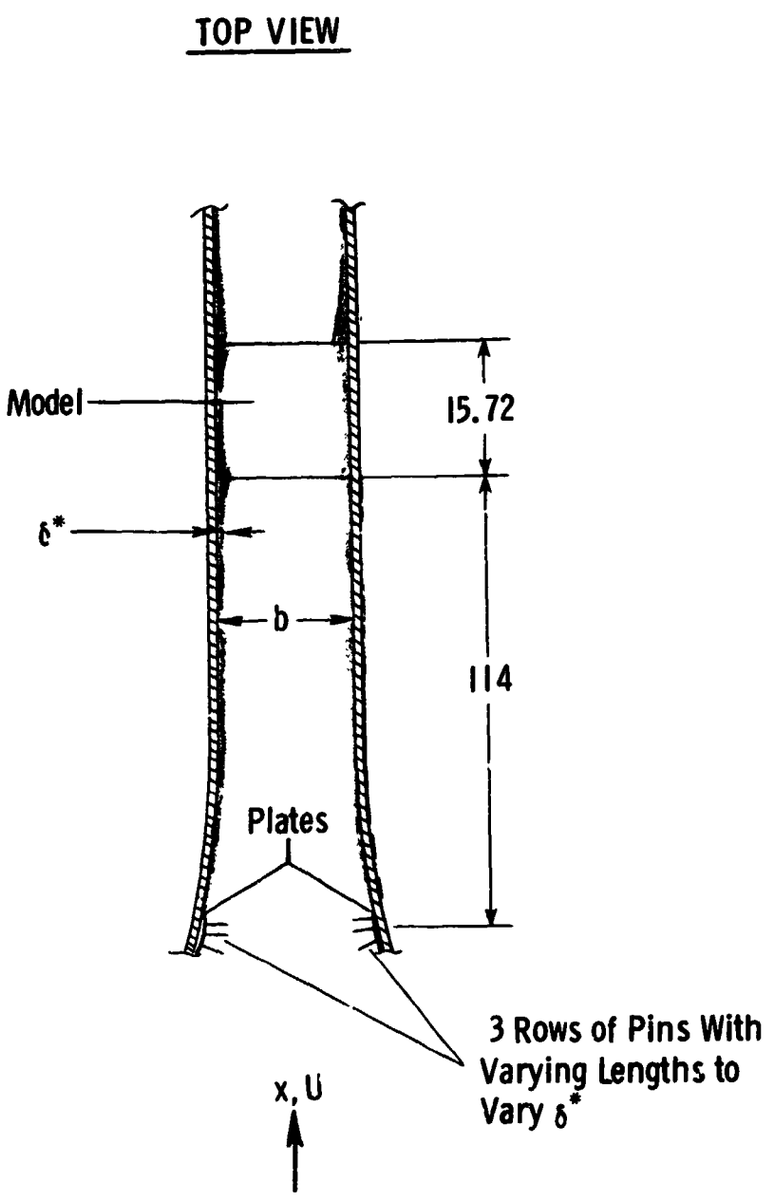

Figure 4.- Experimental apparatus used in the Langley 6- by 19-Inch Transonic Tunnel to investigate the effects of the sidewall boundary-layer displacement thickness on two-dimensional testing. All dimensions are in cm.

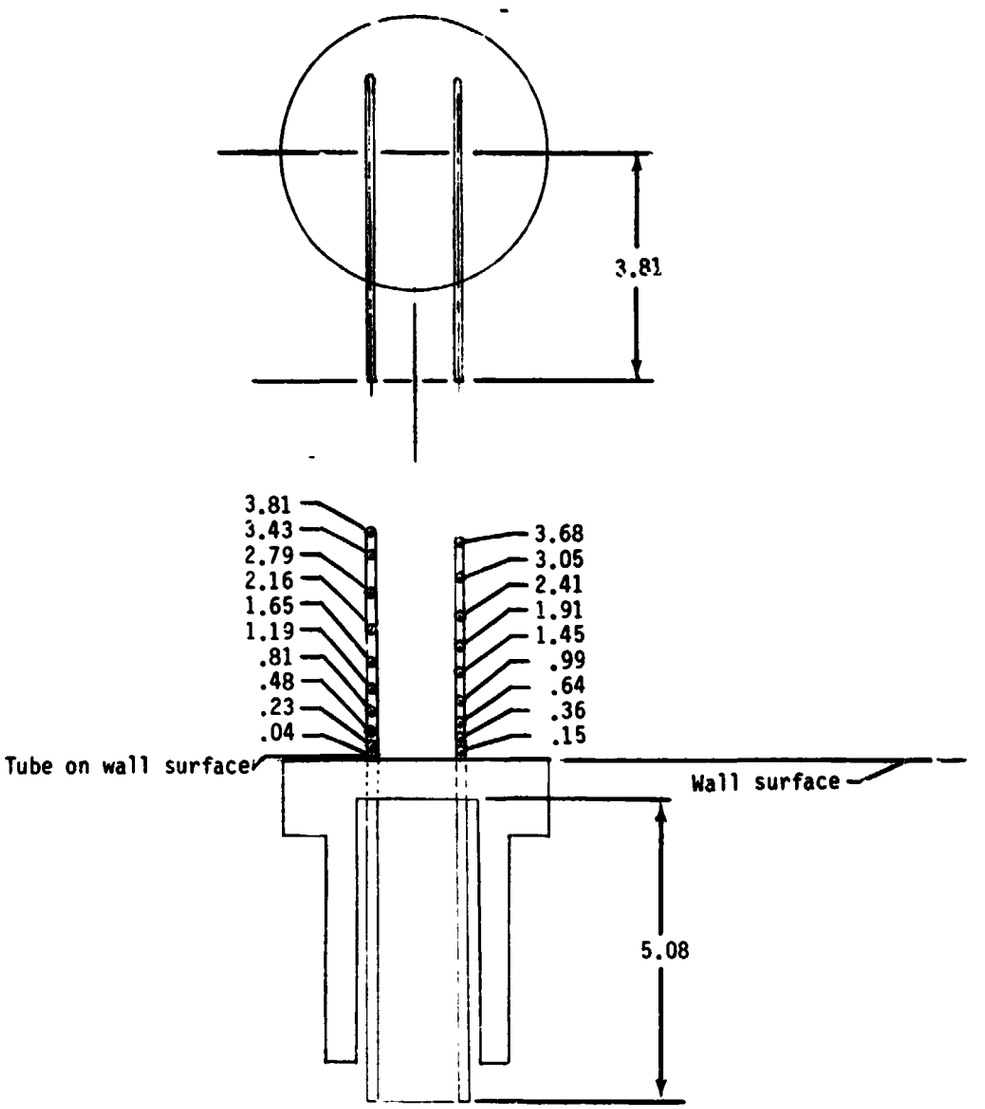

(a) Top and front view.

Figure 5.- Sketch of the rake-tube probes used to survey the sidewall boundary layers in the Langley 6- by 19-Inch Transonic Tunnel All dimensions are in cm.

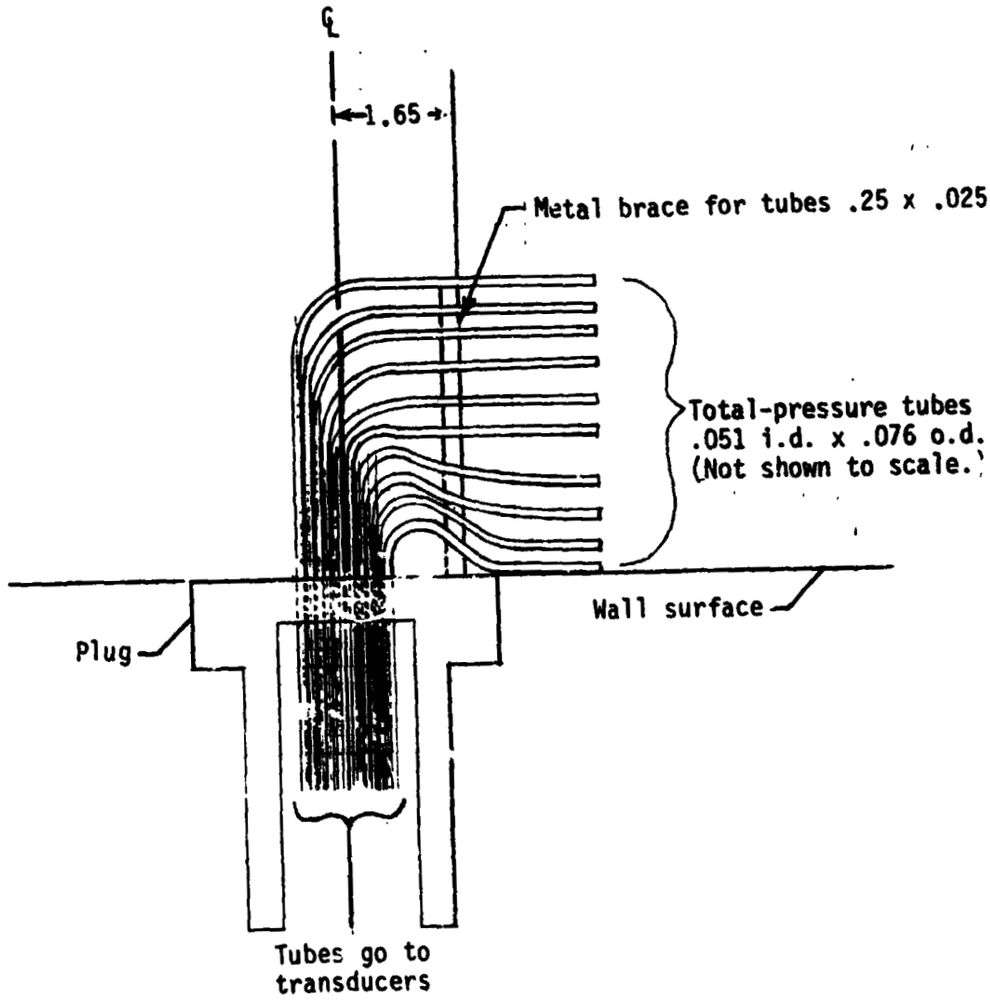

(b) Sideview

Figure 5.- Concluded.

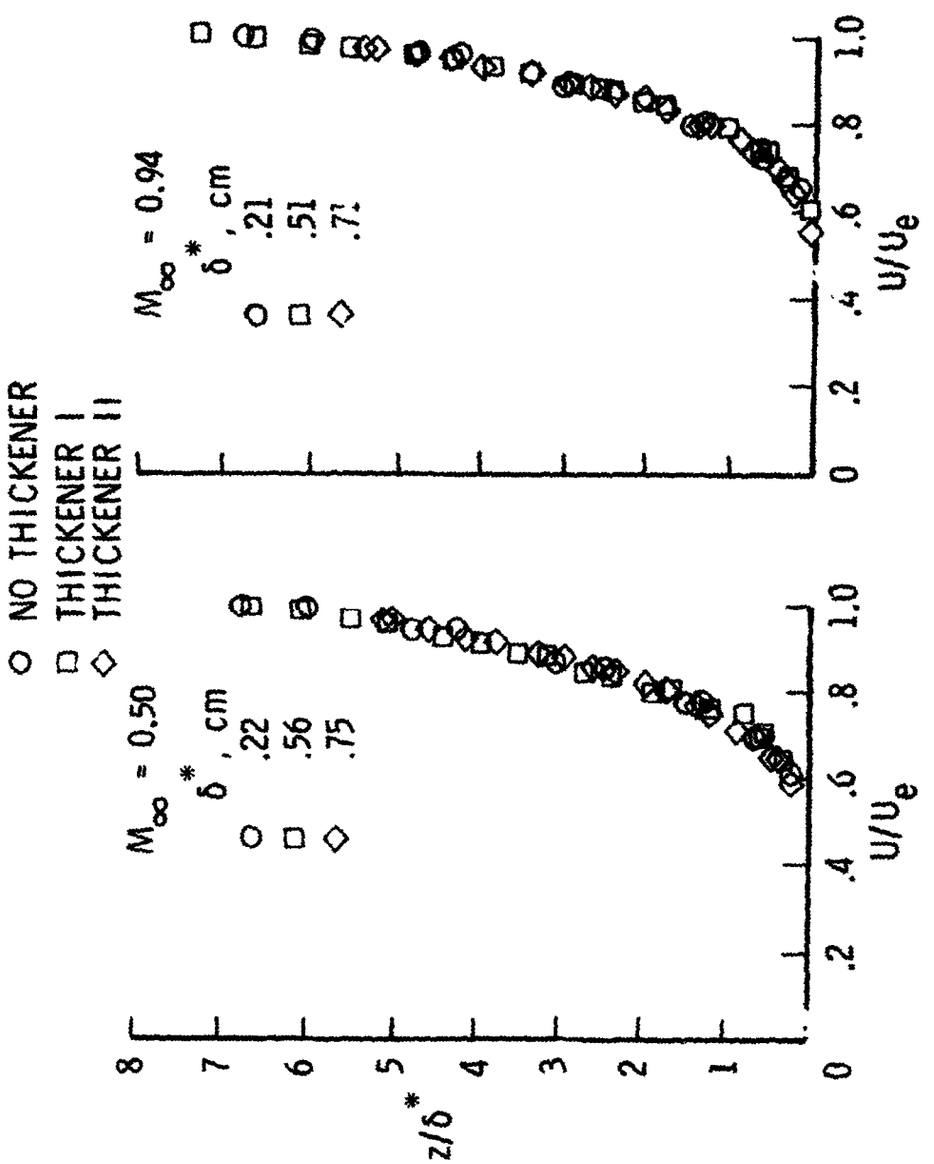

Figure 6.- Nondimensional velocity distribution in artificially thickened sidewall boundary layers.

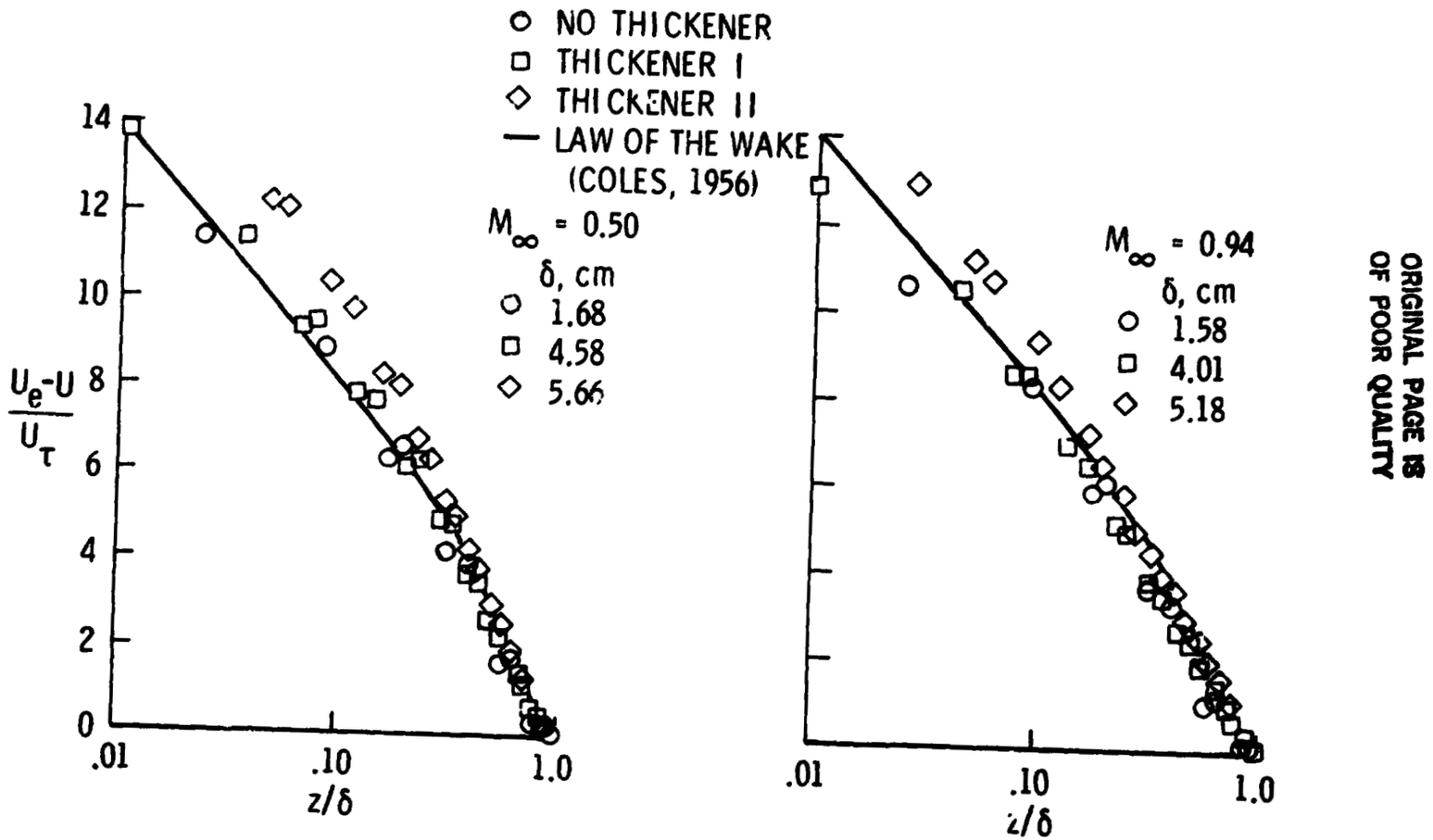

Figure 7.- Nondimensional velocity distributions for law of the wake correlation of artificially thickened sidewall boundary layers.

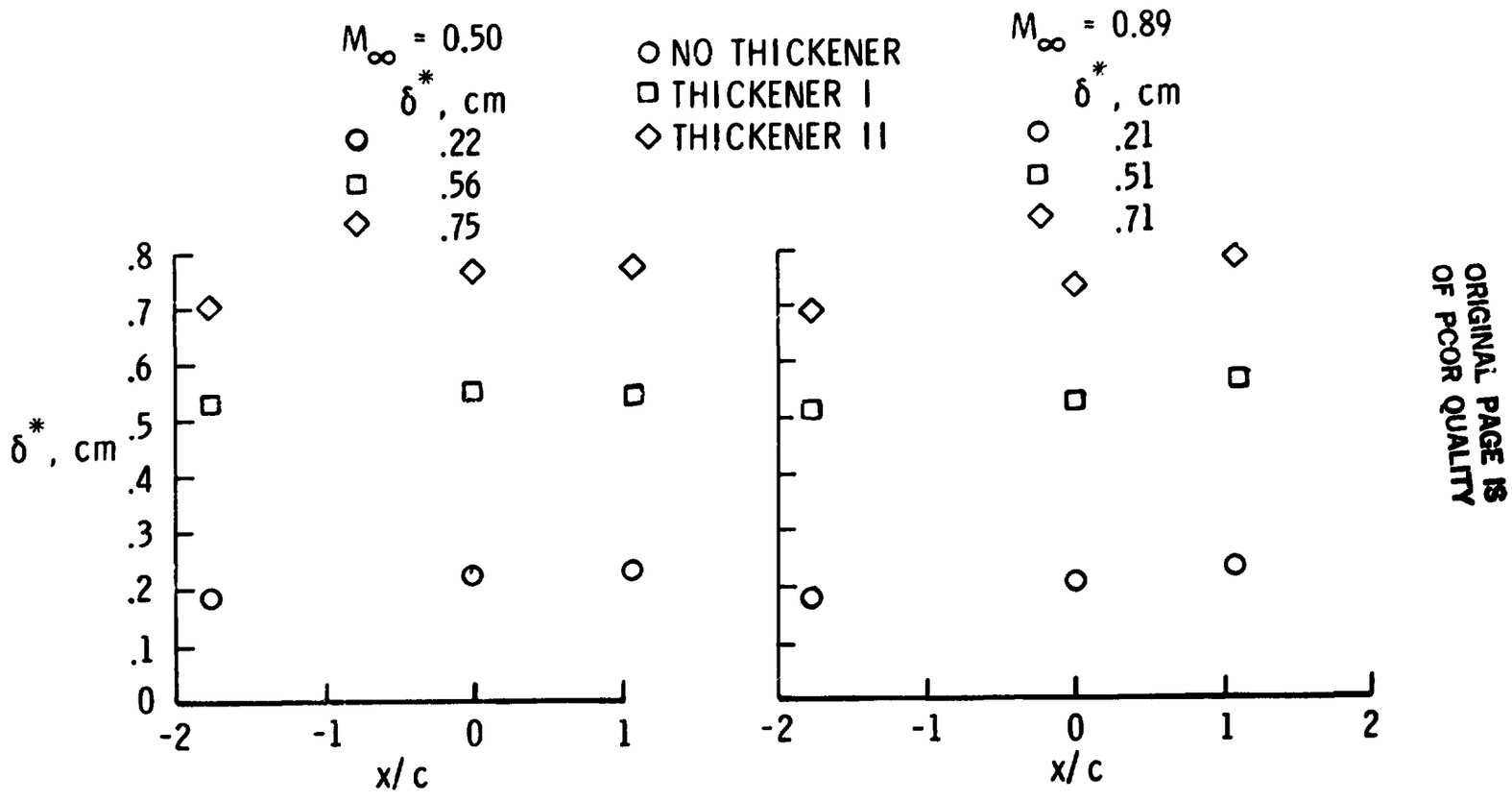

Figure 8.- The variation of the measured boundary-layer displacement thickness near the model station.

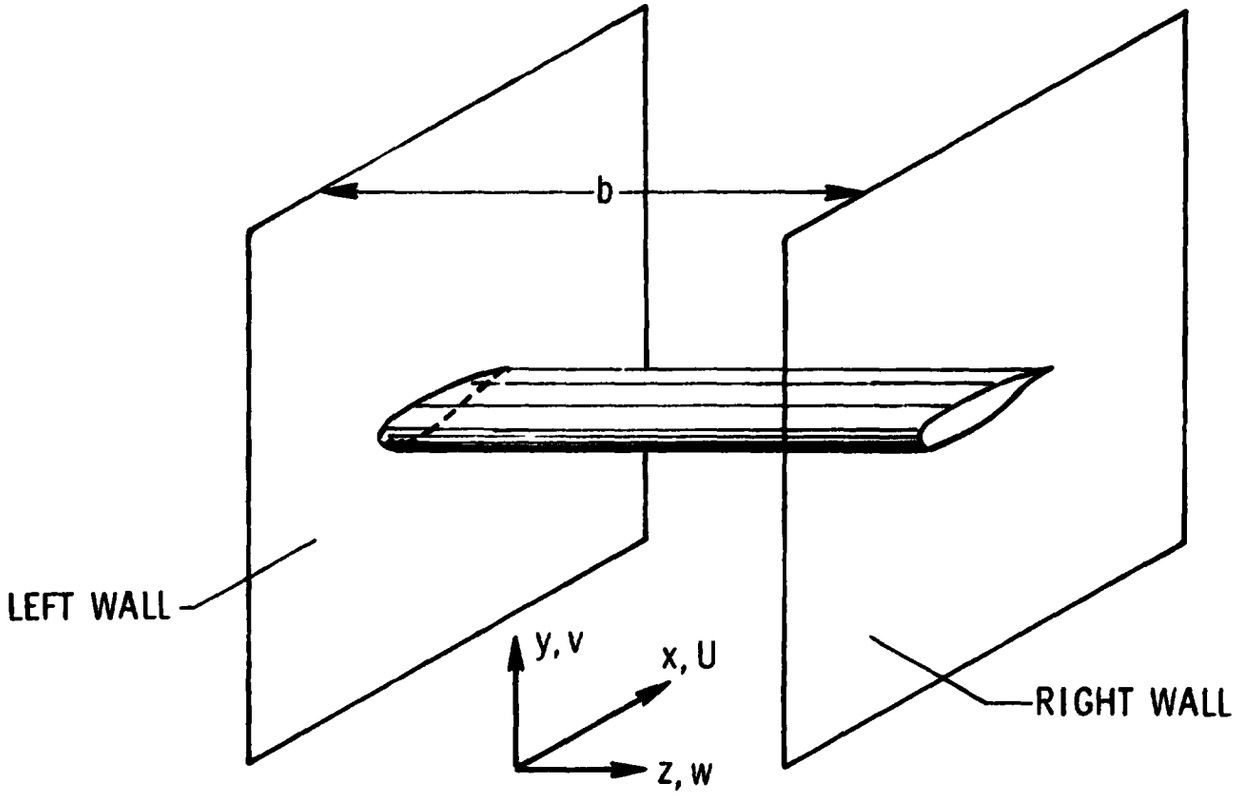

Figure 9.- Sketch of airfoil model and tunnel sidewalls with the coordinate system used.

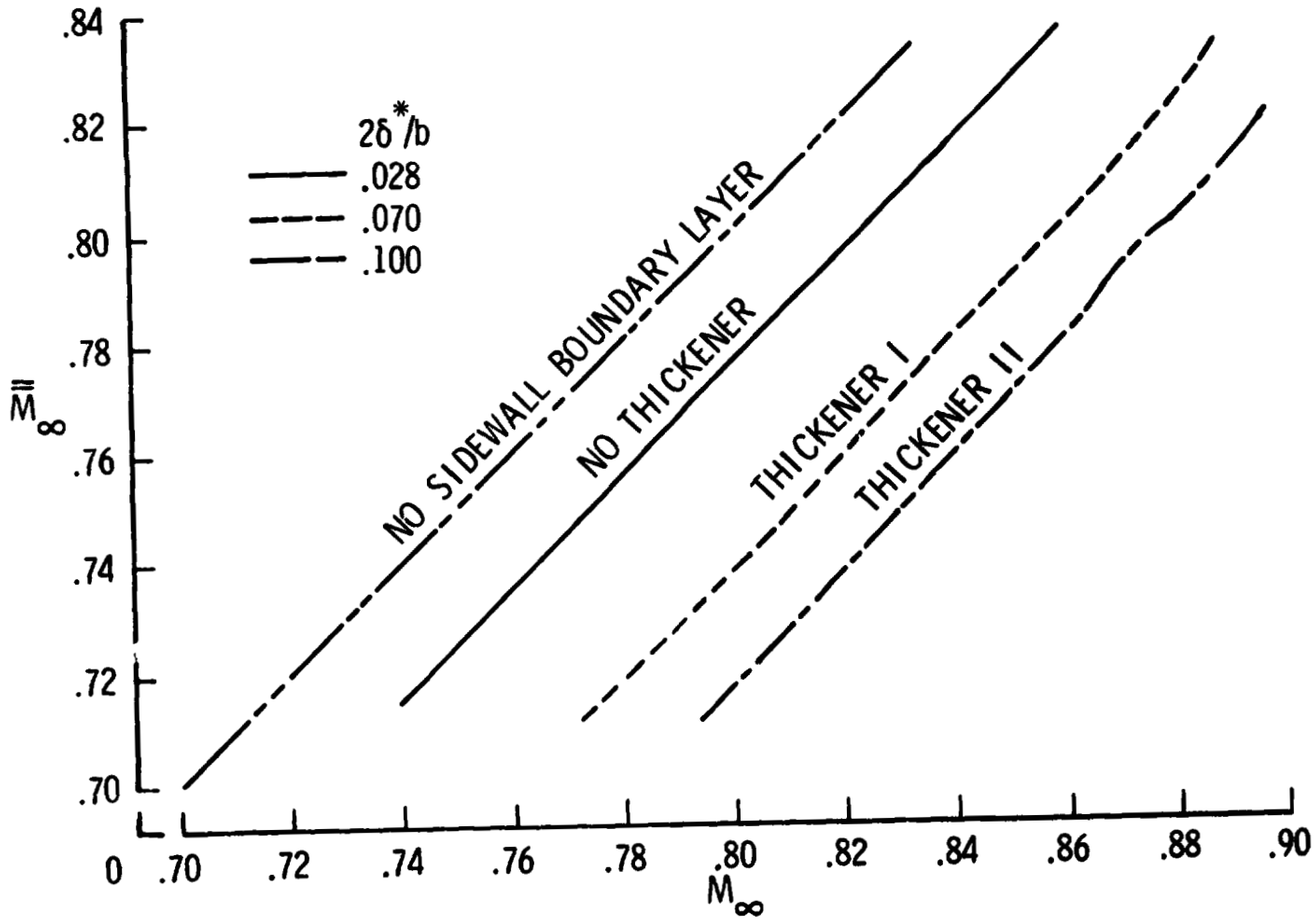

Figure 10.- Variation of equivalent freestream Mach number with measured freestream Mach number for the three sidewall boundary-layer displacement thickness.

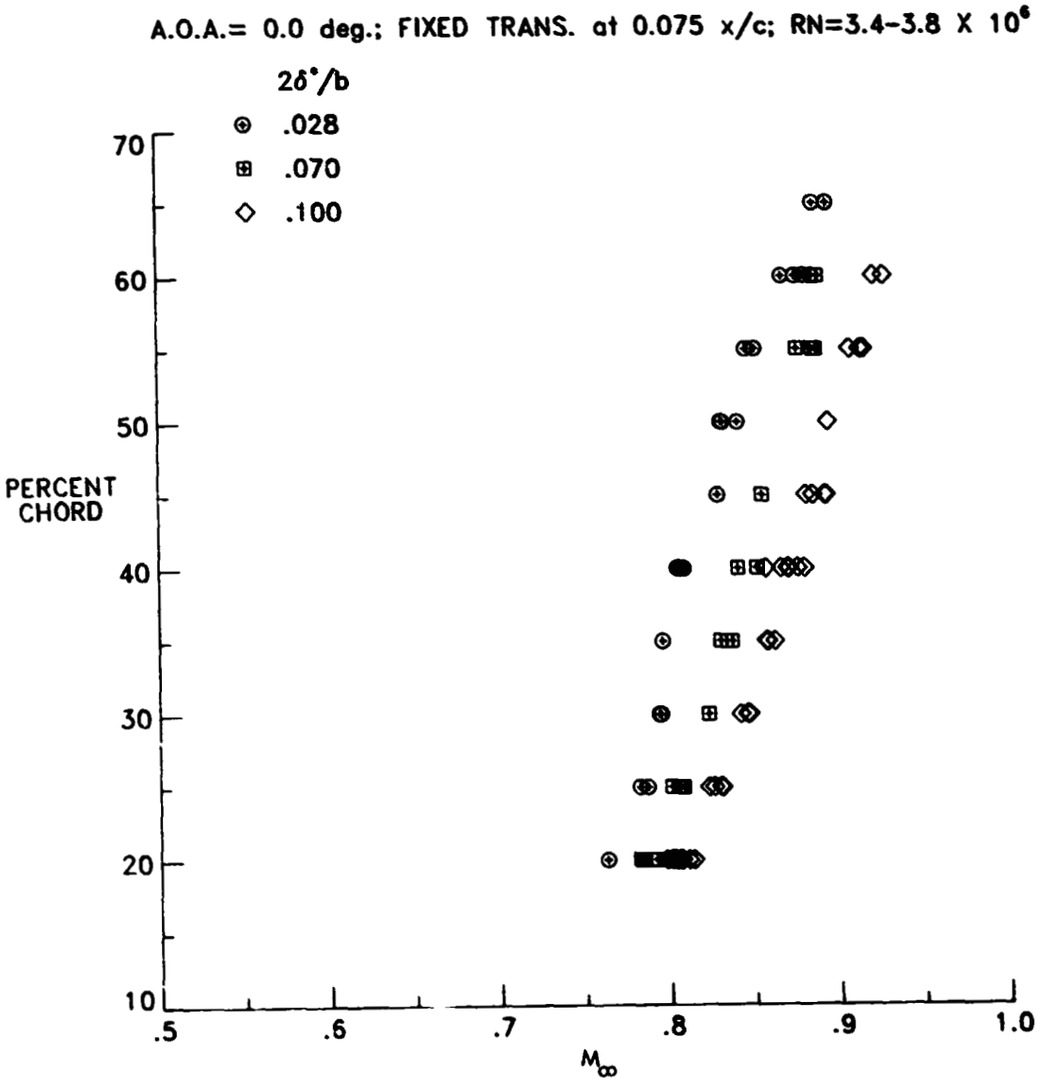

(a) Shock wave location vs. measured freestream Mach number.

Figure 11.- Variation of shock wave location with freestream Mach number for the NACA 0012 airfoil tested with three sidewall boundary-layer displacement thicknesses. Angle of attack is 0 degrees.

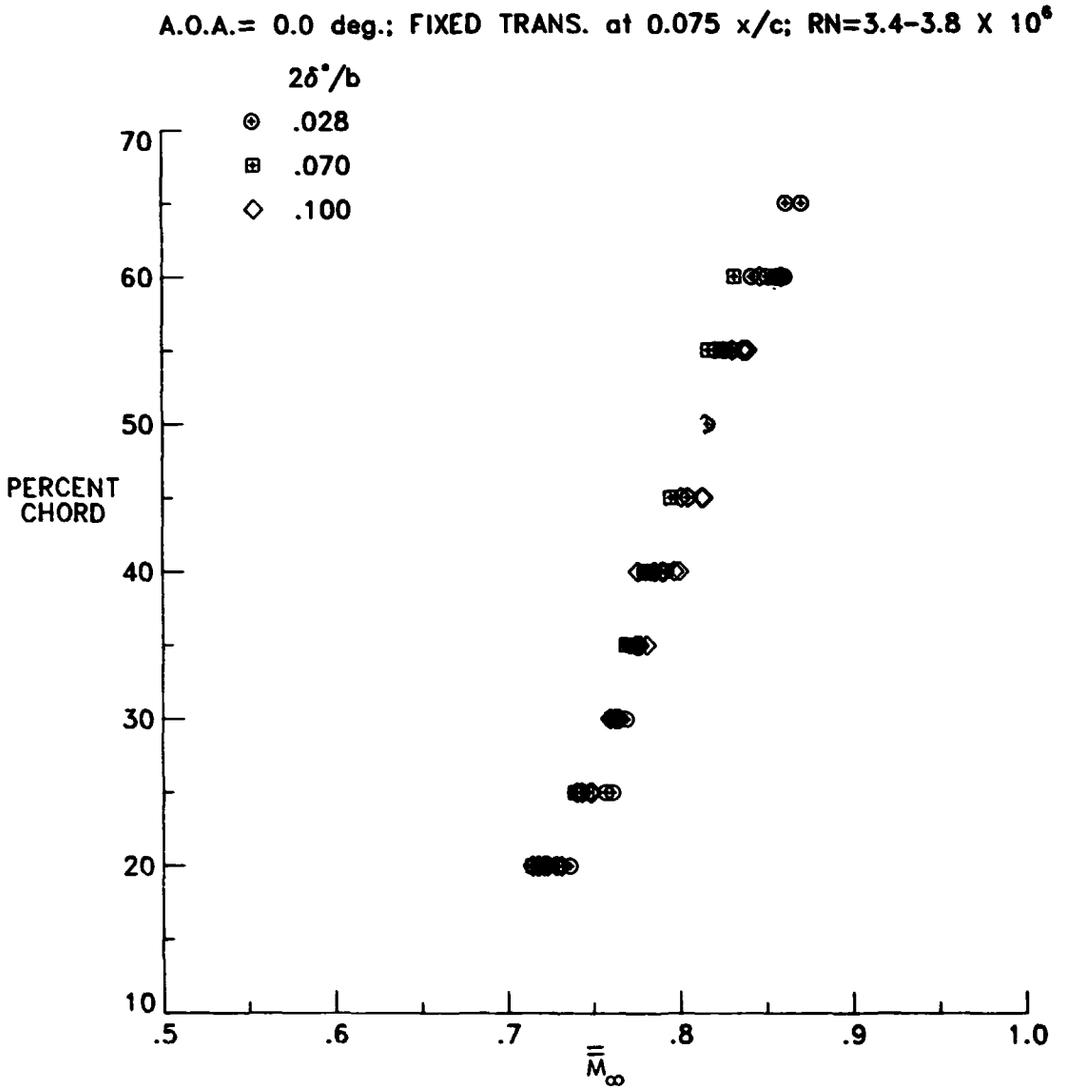

(b) Shock wave location vs. equivalent freestream Mach number.

Figure 11.- Concluded.

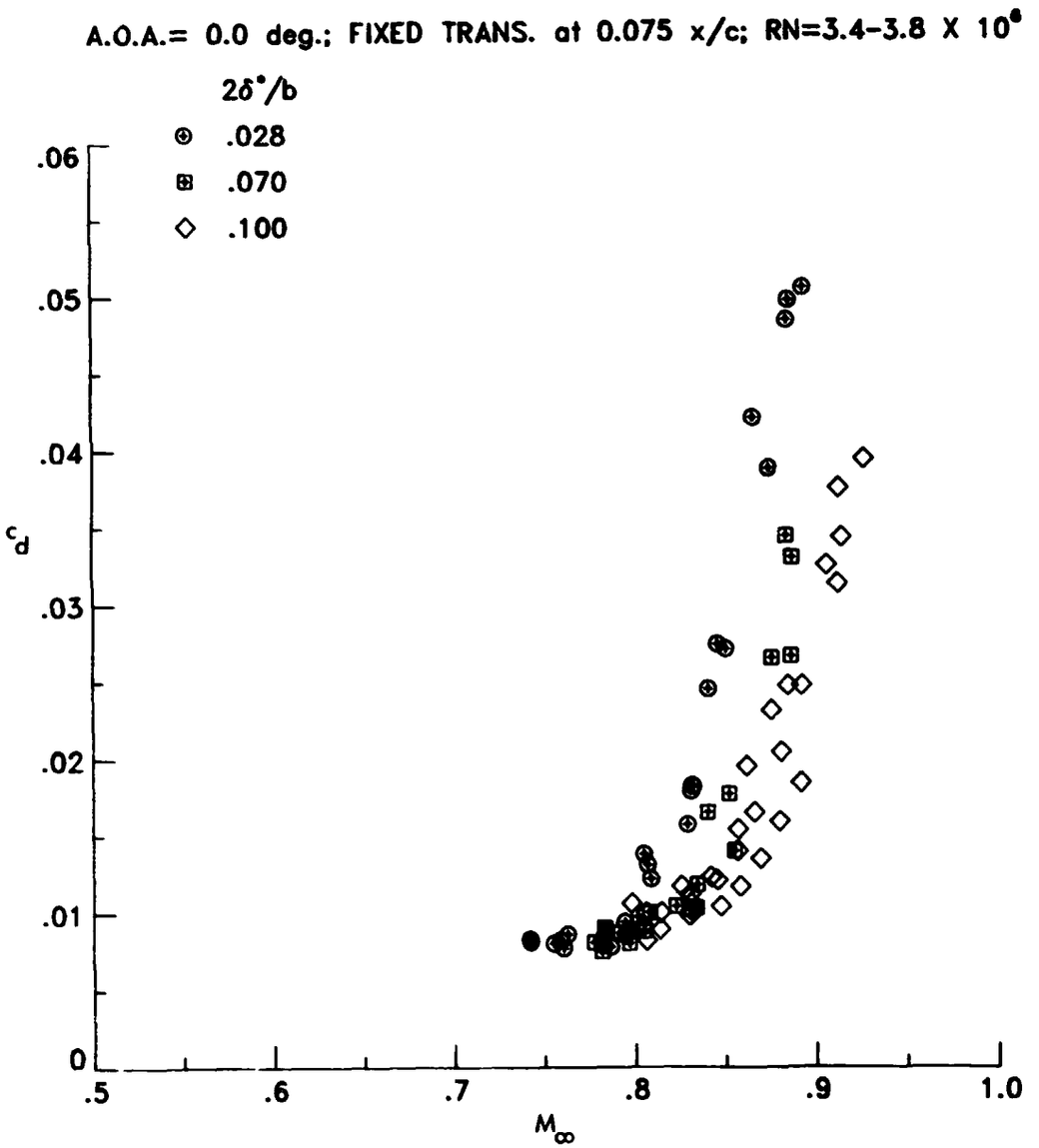

(a) Section drag coefficient vs. measured freestream Mach number.

Figure 12.- Variation of section drag coefficient with freestream Mach number for the NACA 0012 airfoil tested with three sidewall boundary-layer displacement thicknesses. Angle of attack is (degrees.

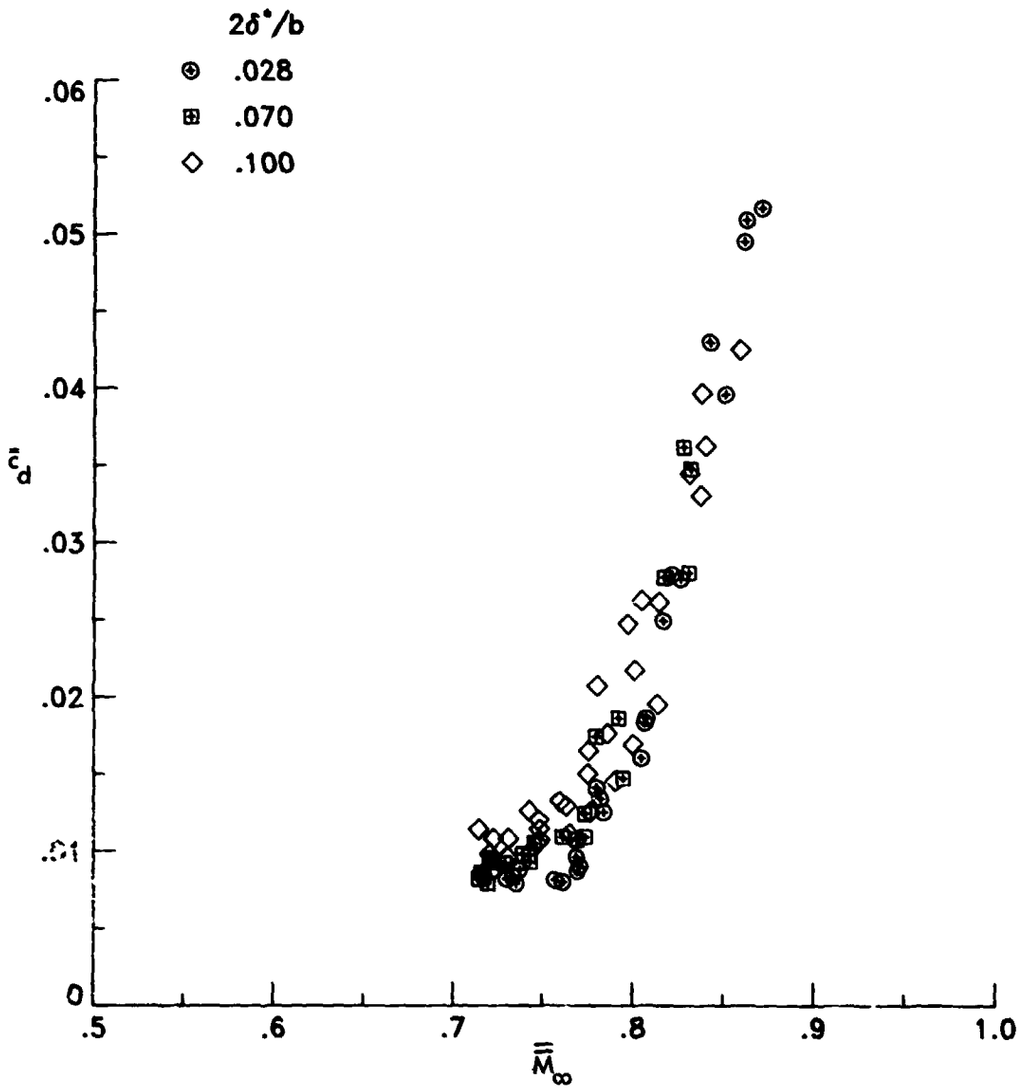

(b) Adjusted section drag coefficient vs. equivalent freestream Mach number.

Figure 12.- Concluded.

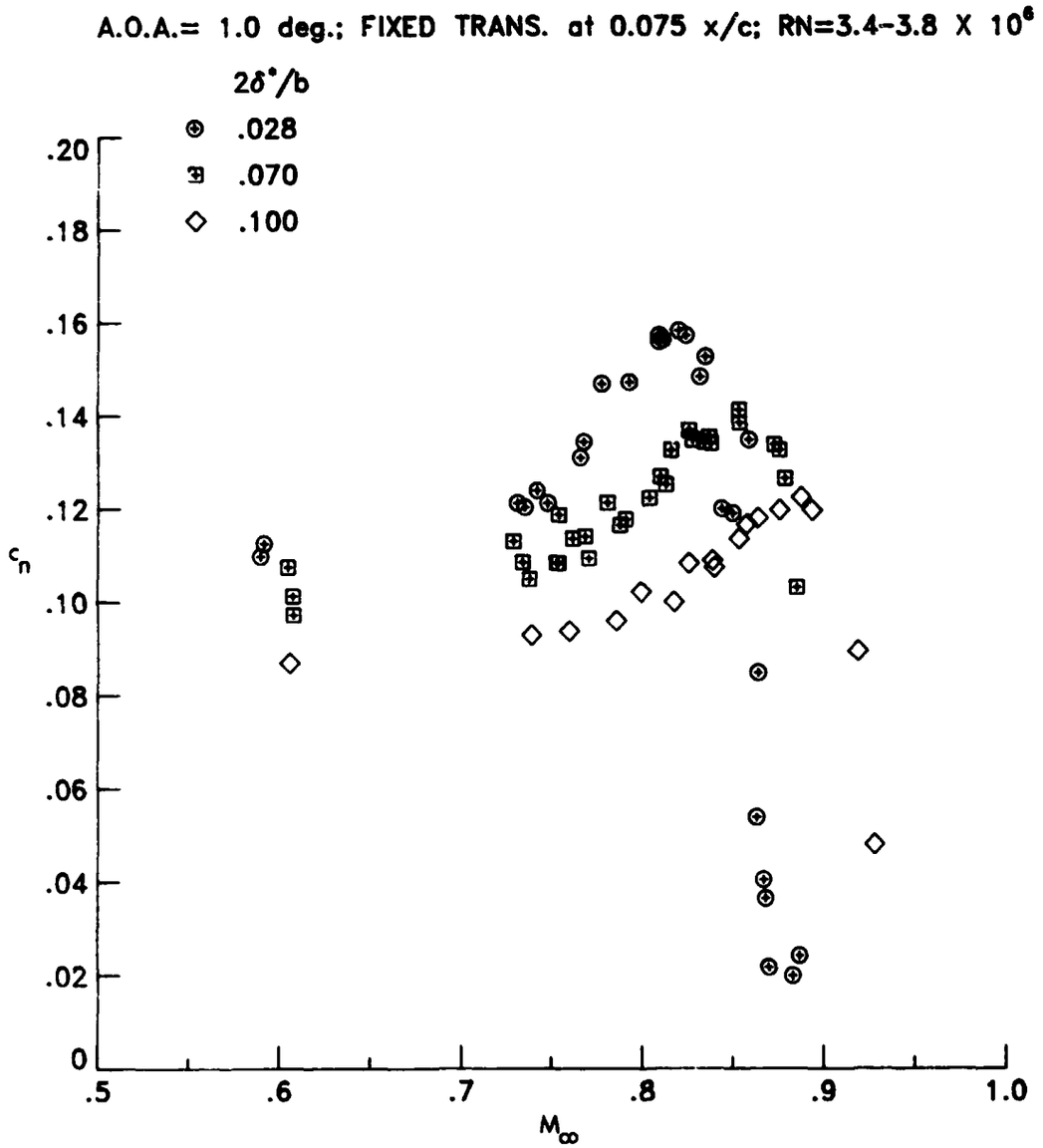

(a) Normal-force coefficient vs. measured freestream Mach number.

Figure 13.- Variation of normal-force coefficient with freestream Mach number for the NACA 0012 airfoil tested with three sidewall boundary-layer displacement thicknesses. Angle of attack is 1.0 degree.

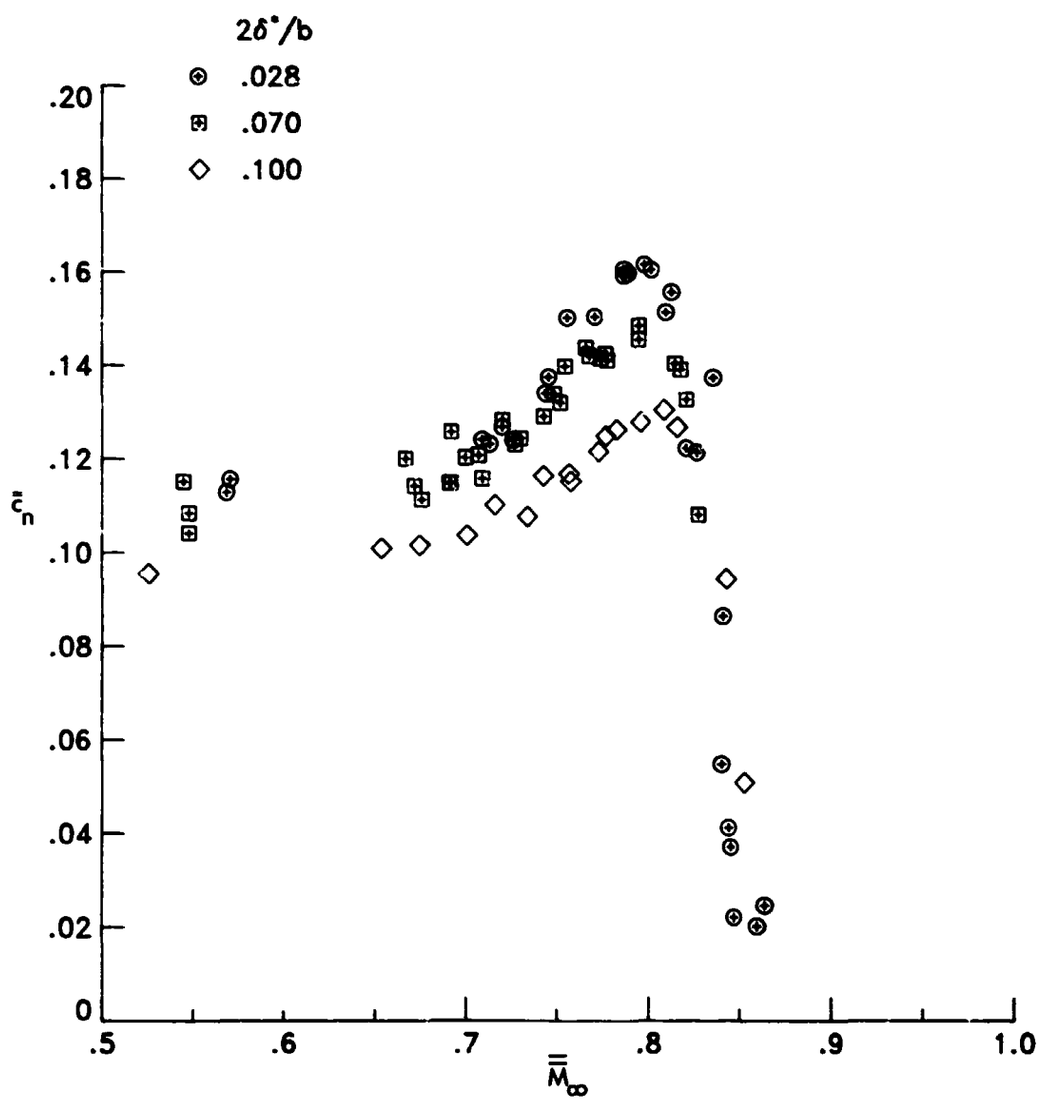

(b) Adjusted normal-force coefficient vs. equivalent freestream Mach number.

Figure 13.- Concluded.

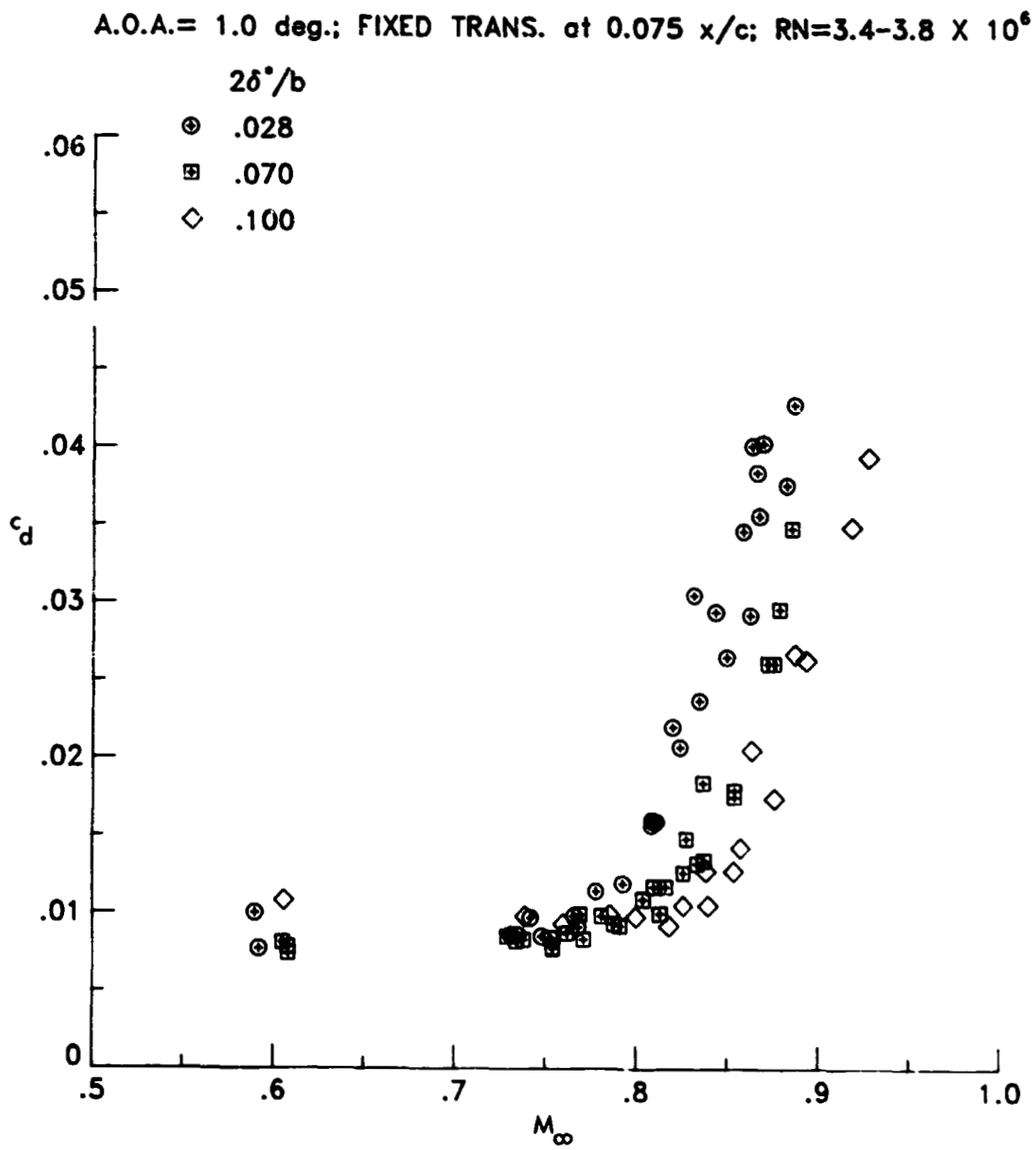

(a) Section drag coefficient vs. measured freestream Mach number.

Figure 14.- Variation of section drag coefficient with freestream Mach number for the NACA 0012 airfoil tested with three sidewall boundary-layer displacement thicknesses. Angle of attack is 1.0 degree.

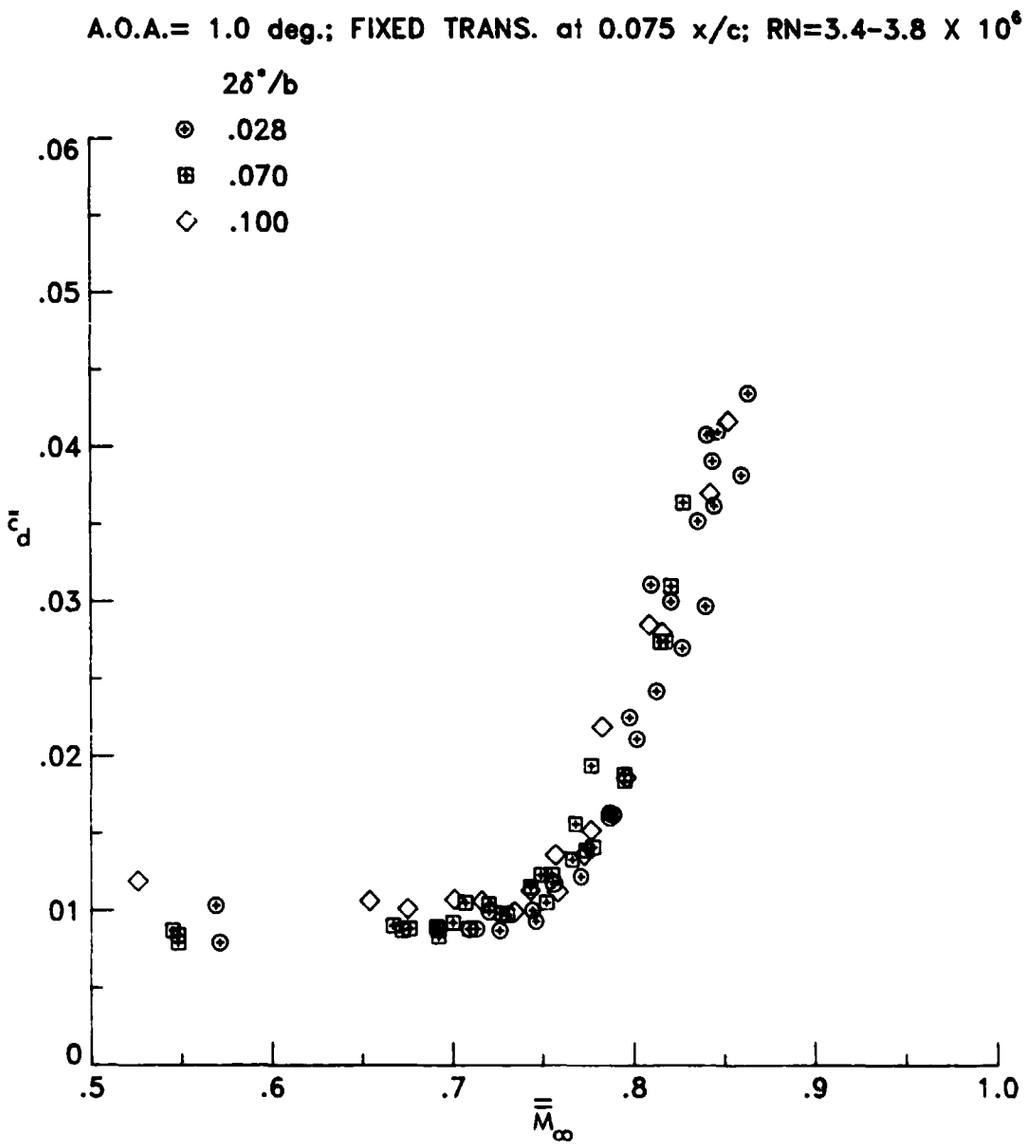

(b) Adjusted section drag coefficient vs. equivalent freestream Mach number.

Figure 14.- Concluded.

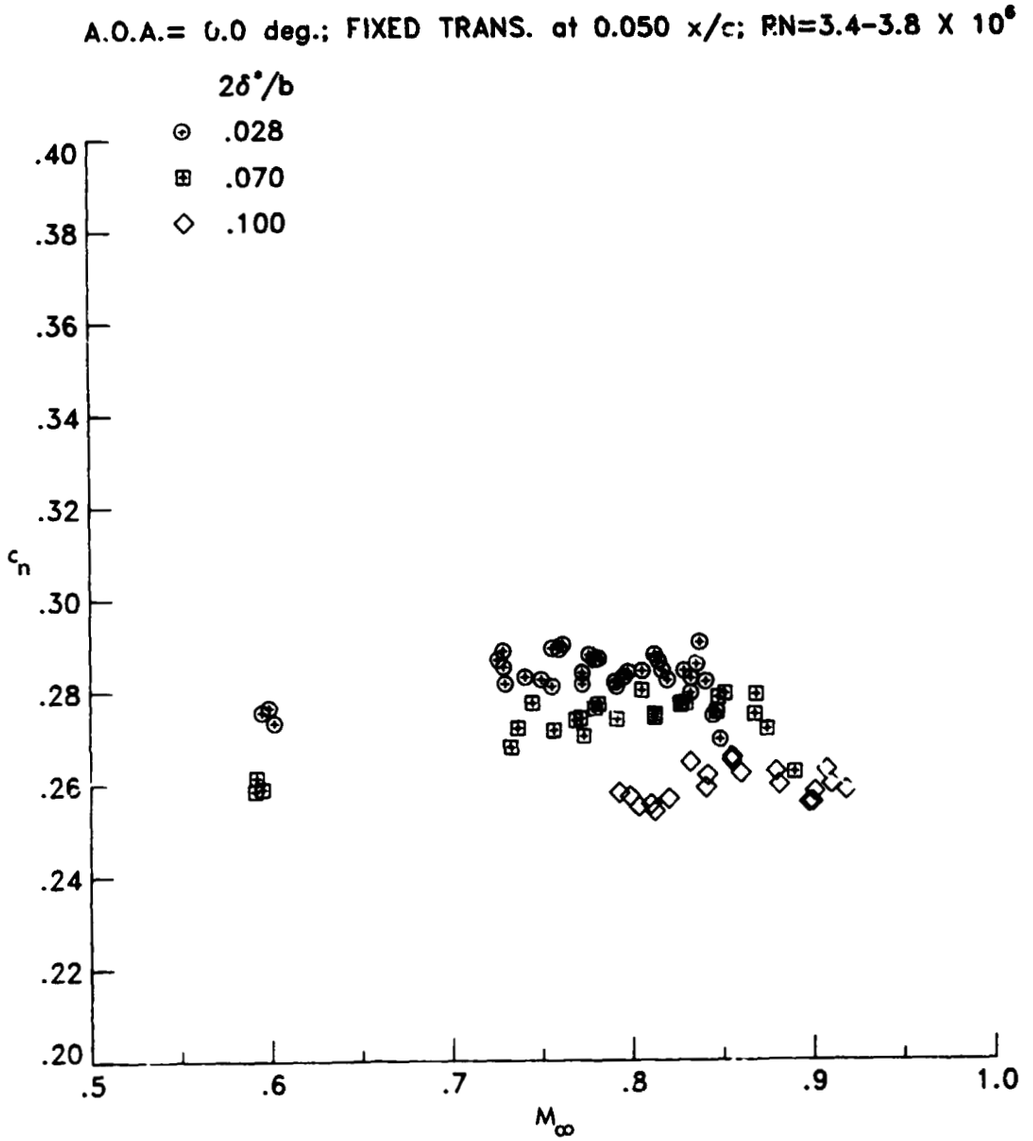

(a) Normal-force coefficient vs. measured freestream Mach number.

Figure 15.- Variation of normal-force coefficient with freestream Mach number for the SC-27 airfoil tested with three sidewall boundary-layer displacement thicknesses. Angle of attack is 0 degrees.

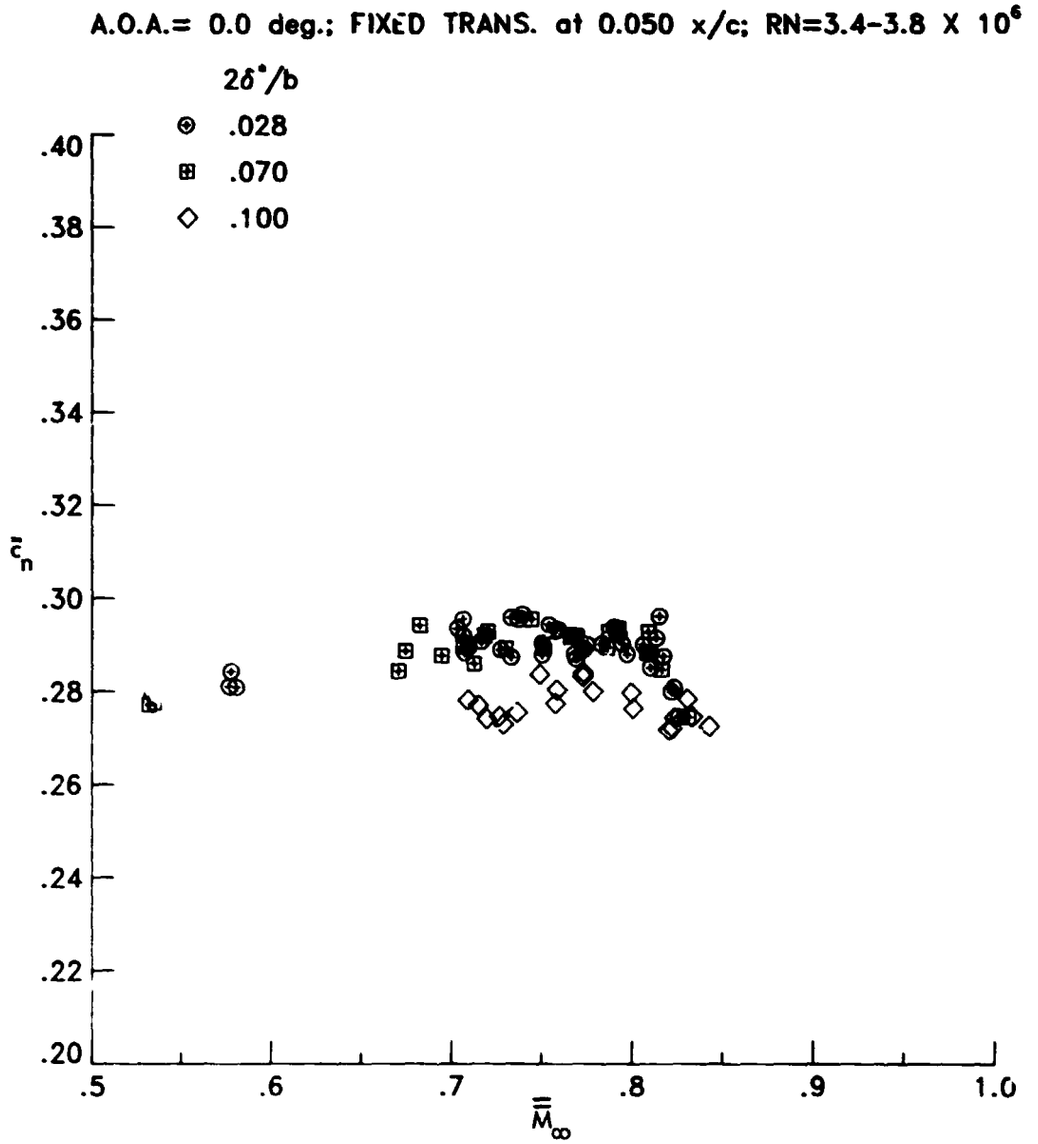

(b) Adjusted normal-force coefficient with equivalent freestream Mach number.

Figure 15.- Concluded.

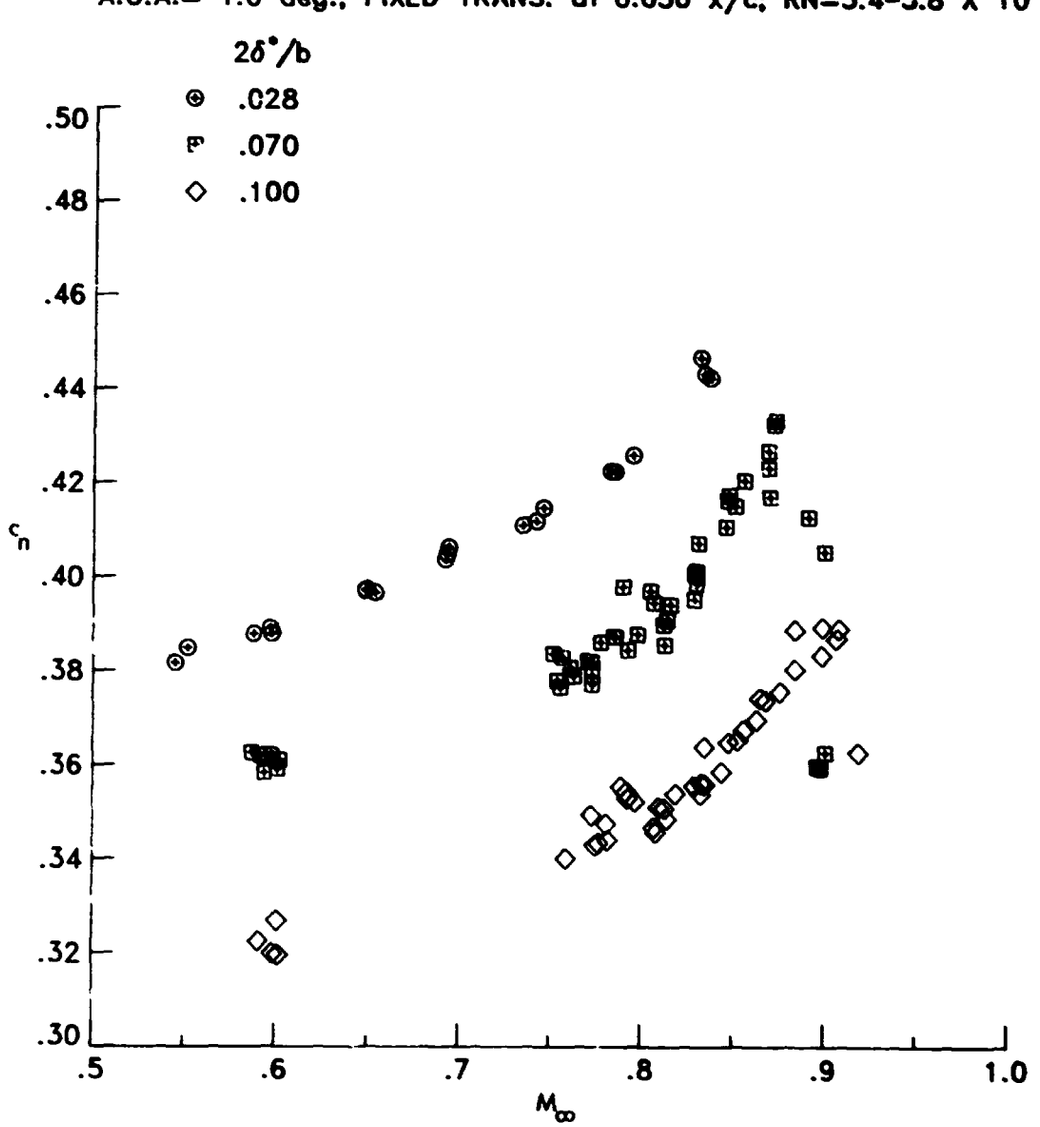

(a) Normal-force coefficient vs. measured freestream Mach number.

Figure 16.- Variation of normal-force coefficient with freestream Mach number for the SC-27 airfoil tested with three sidewall boundary-layer displacement thicknesses. Angle of attack is 1.0 degree.

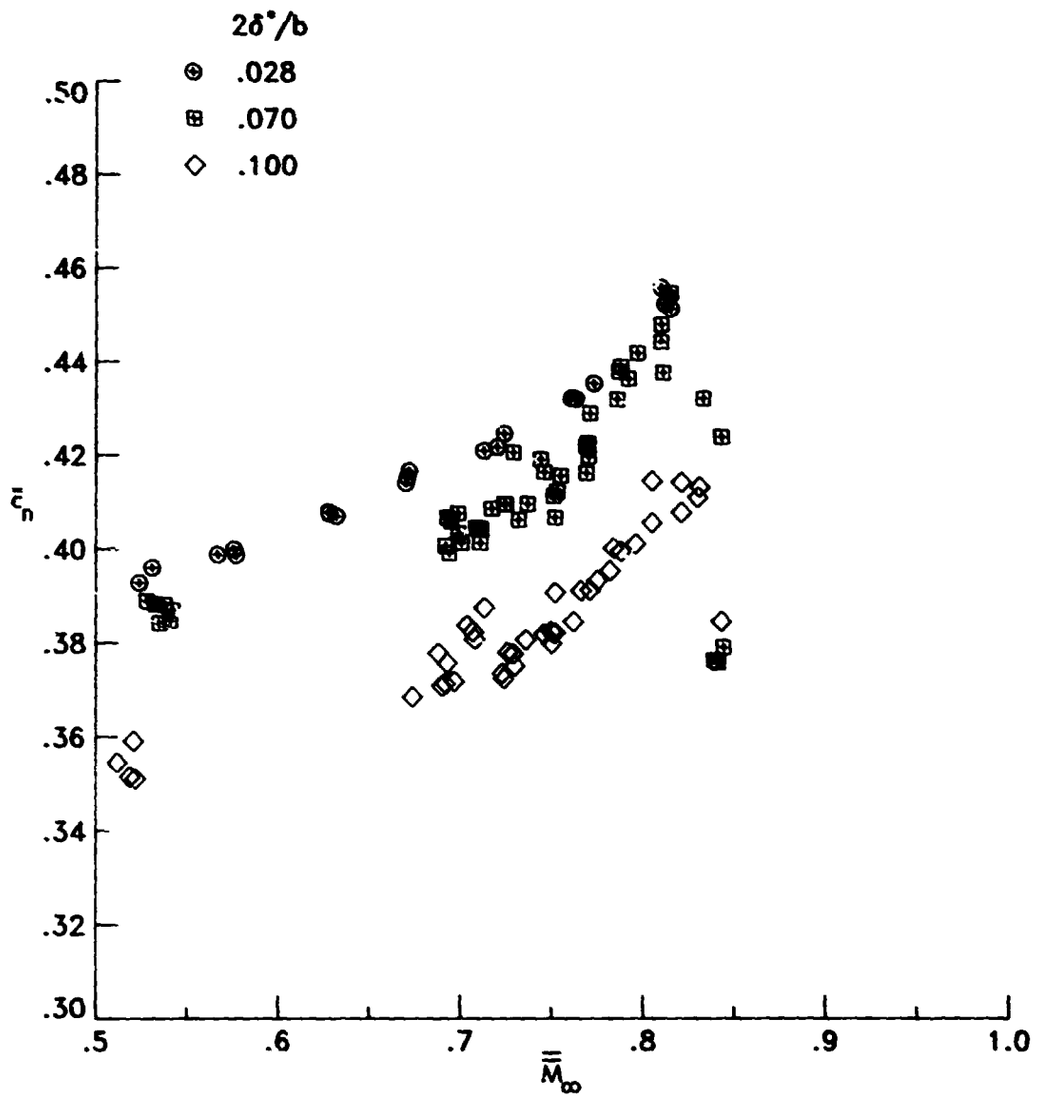

(b) Adjusted normal-force coefficient vs. equivalent freestream Mach number.

Figure 16.- Concluded.

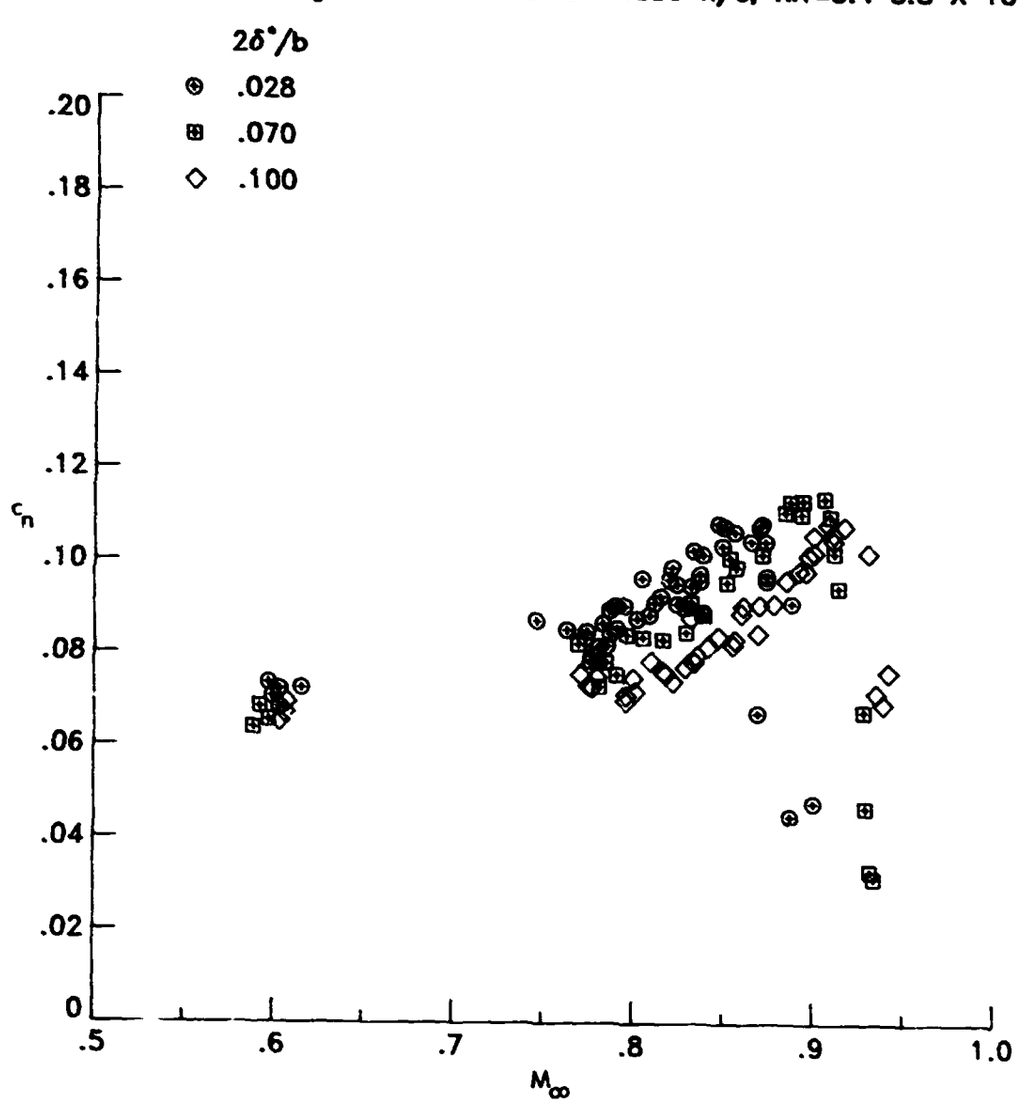

(a) Normal-force coefficient vs. measured freestream Mach number.

Figure 17.- Variation of normal-force coefficient with freestream Mach number for the NLR-1 airfoil tested with three sidewall boundary-layer displacement thicknesses. Angle of attack is 0 degrees.

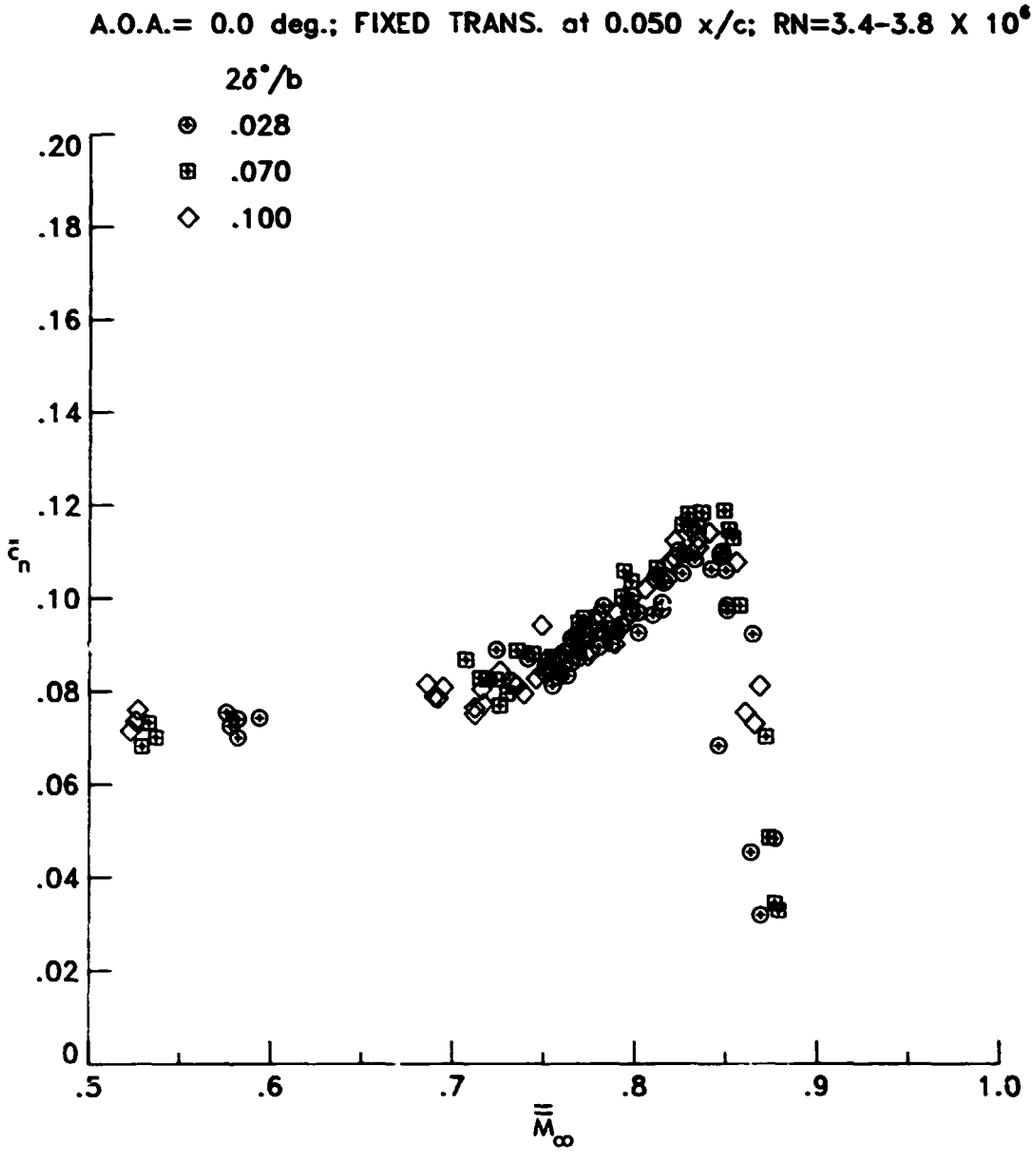

(b) Adjusted normal-force coefficient vs. equivalent freestream Mach number.

Figure 17.- Concluded.

LOCAL MACH NUMBER DISTRIBUTIONS ON NLR-1 AIRFOIL A.O.A.= 0.0 DEG., FIXED TRANS. AT 0.05 X/C

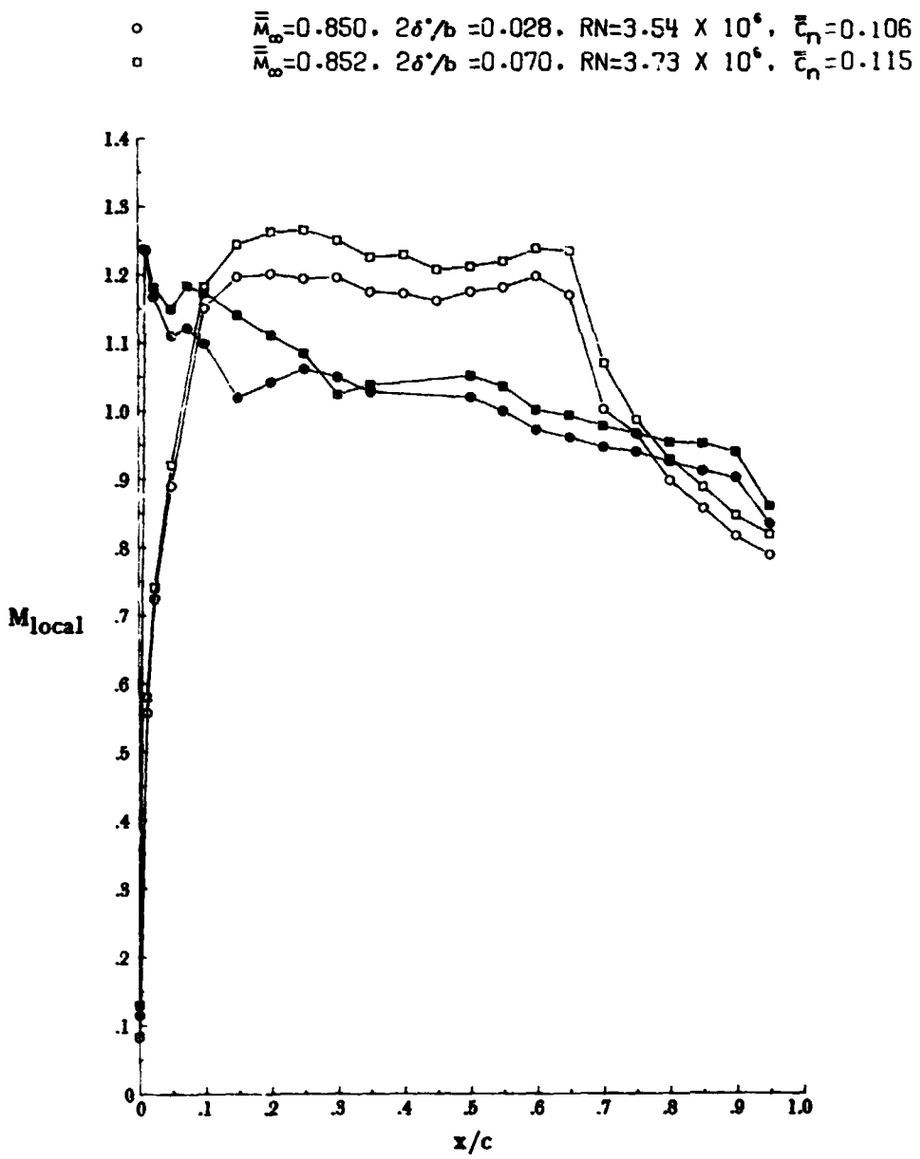

(a) $\bar{M} \simeq 0.85$

Figure 18.- Chordwise local Mach number distributions on the NLR-1 airfoil. Angle of attack is 0.0 degrees. Open symbols indicate the airfoil upper surface; centered symbols indicate the airfoil lower surface.

LOCAL MACH NUMBER DISTRIBUTIONS ON NLR-1 AIRFOIL A.O.A.= 0.0 DEG., FIXED TRANS. AT 0.05 X/C

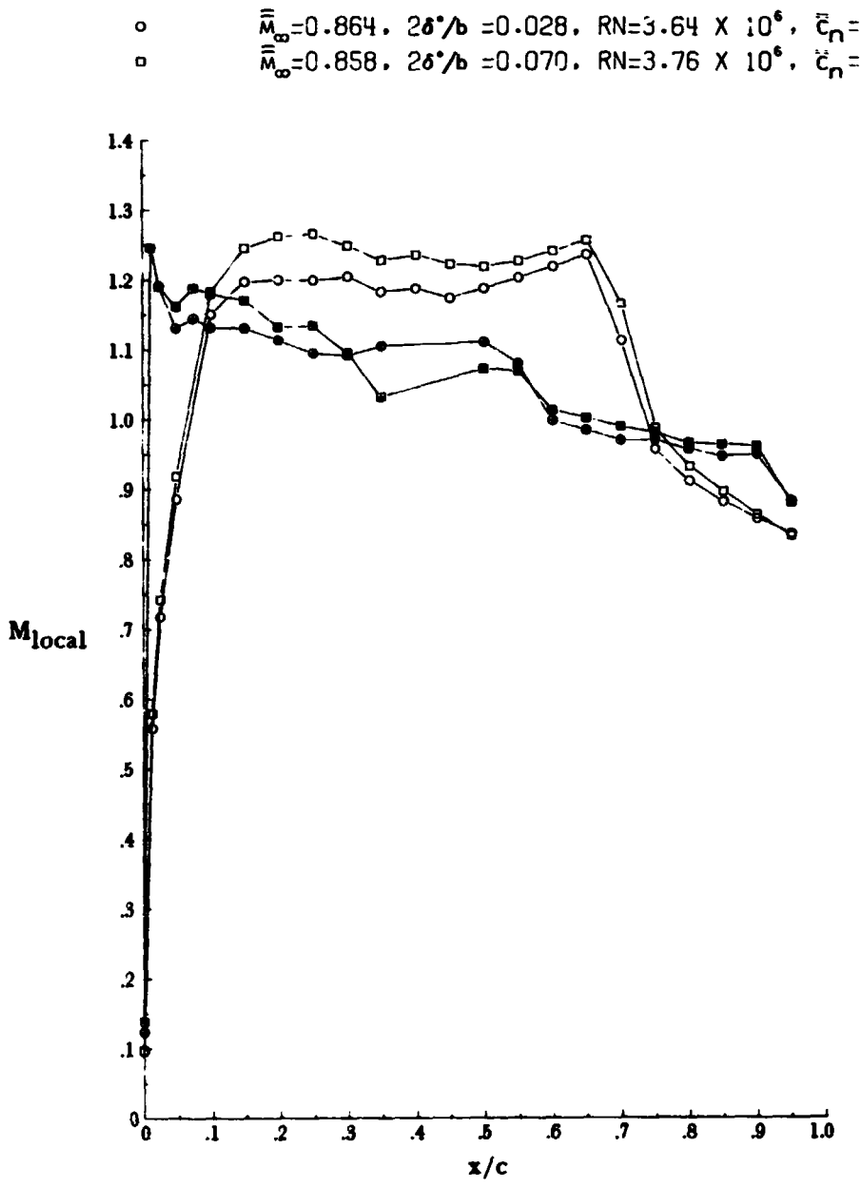

(b) $\bar{\bar{M}}_\infty$ = 0.86

Figure 18.- Concluded.

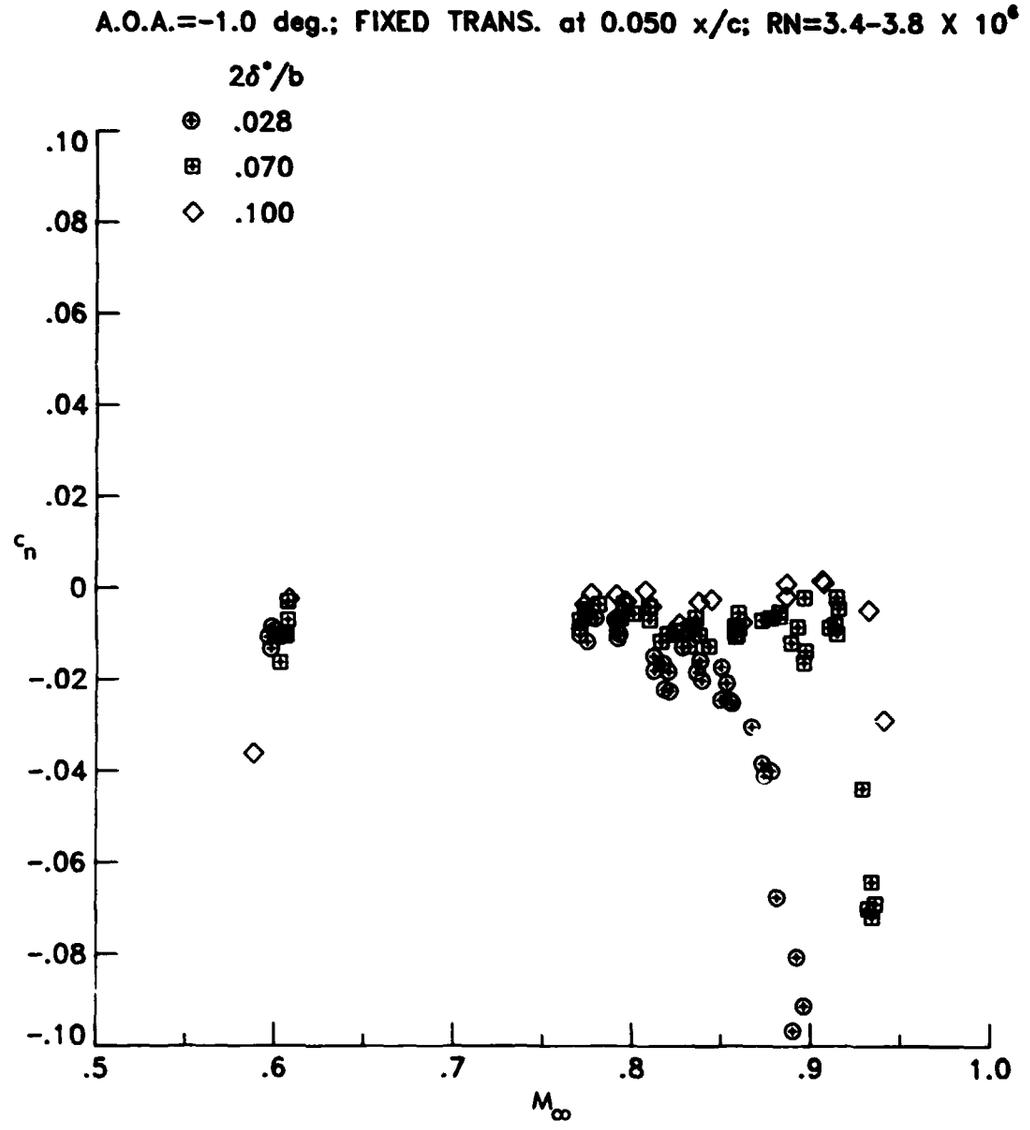

(a) Normal-force coefficient vs. measured freestream Mach number.

Figure 19.- Variation of normal-force coefficient with freestream Mach number for the NLR-1 airfoil tested with three sidewall boundary-layer displacement thicknesses. Angle of attack is -1.0 degree.

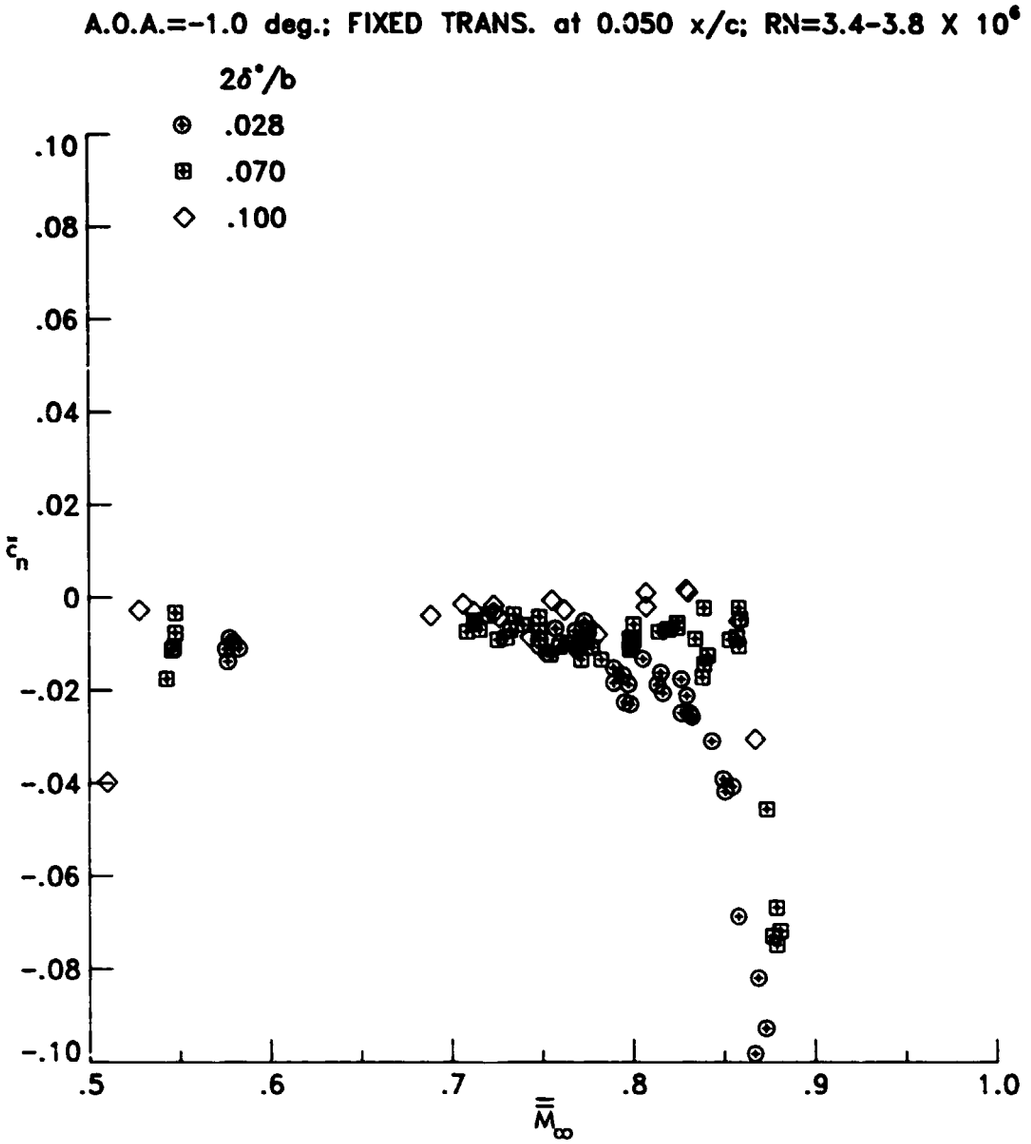

(b) Adjusted normal-force coefficient vs. equivalent freestream Mach number.

Figure 19.- Concluded.

LOCAL MACH NUMBER DISTRIBUTIONS ON NLR-1 AIRFOIL A.O.A.=-1.0 DEG., FIXED TRANS. AT 0.05 X/C

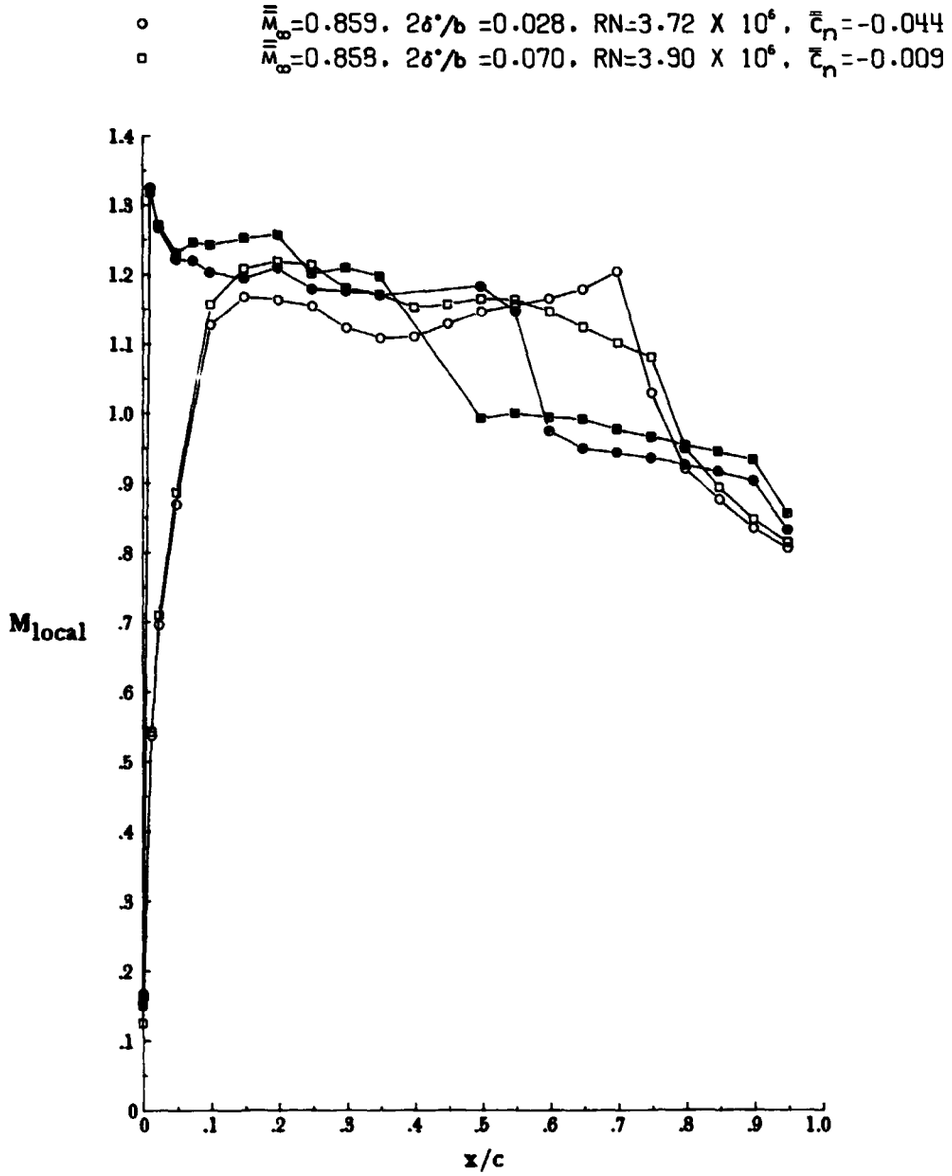

Figure 20.- Chordwise local Mach number distributions on the NLR-1 airfoil. Angle of attack is -1.0 degree. Open symbols indicate the airfoil upper surface; centered symbols indicate the airfoil lower surface.

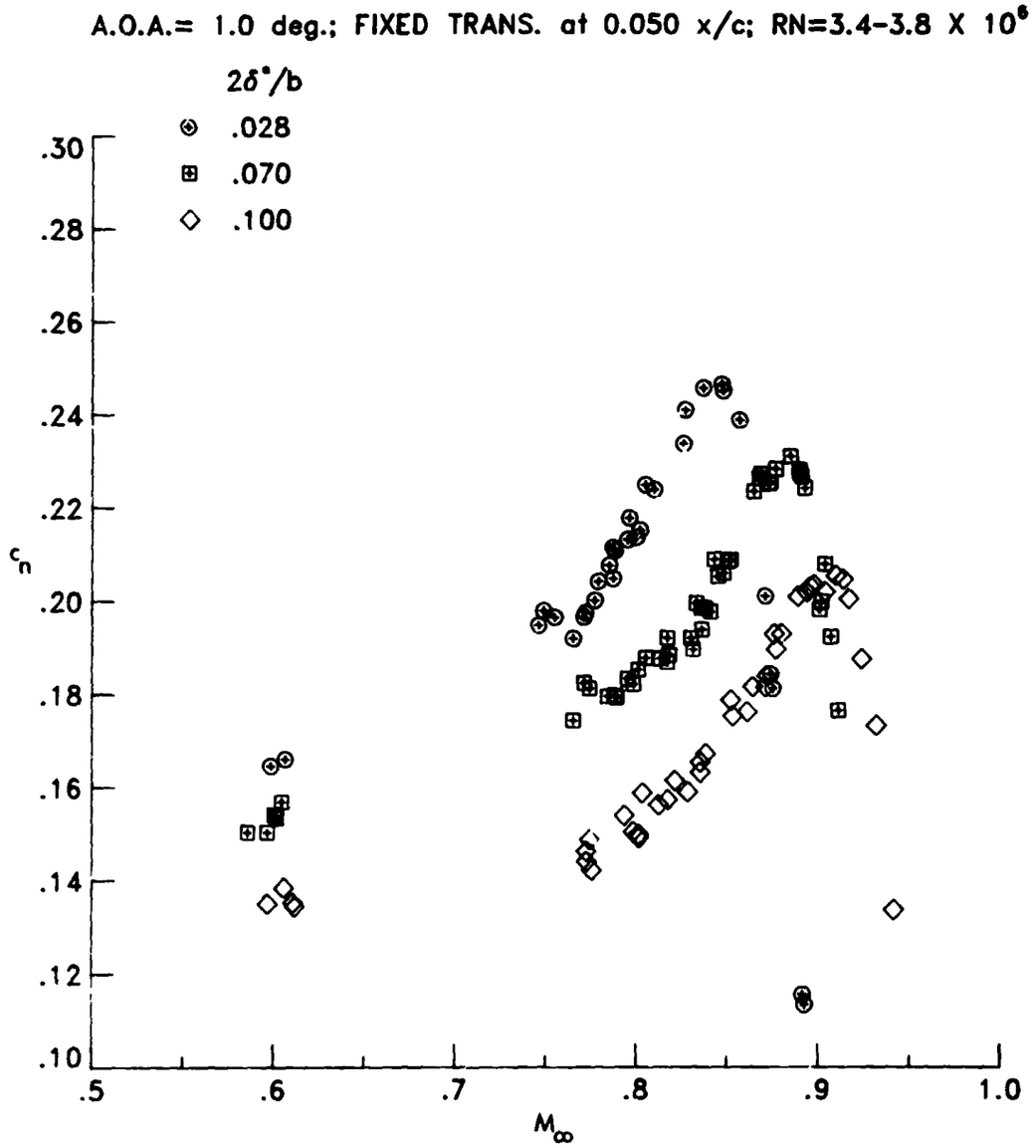

(a) Normal-force coefficient vs. measured freestream Mach number.

Figure 21.- Variation of normal-force coefficient with freestream Mach number for the NLR-1 airfoil tested with three sidewall boundary-layer displacement thicknesses. Angle of attack is 1.0 degree.

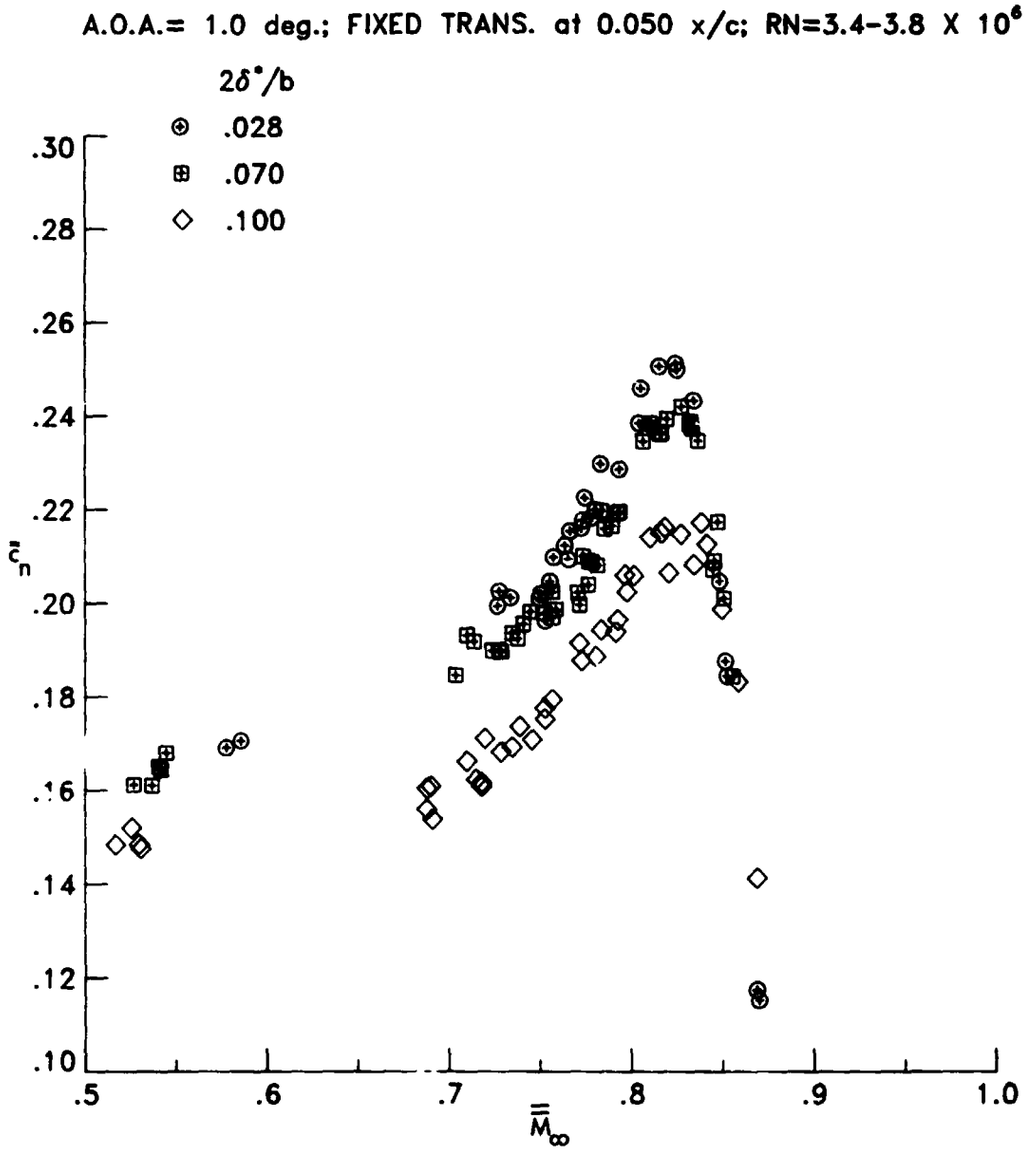

(b) Adjusted normal-force coefficient vs. equivalent freestream Mach number.

Figure 21.- Concluded.

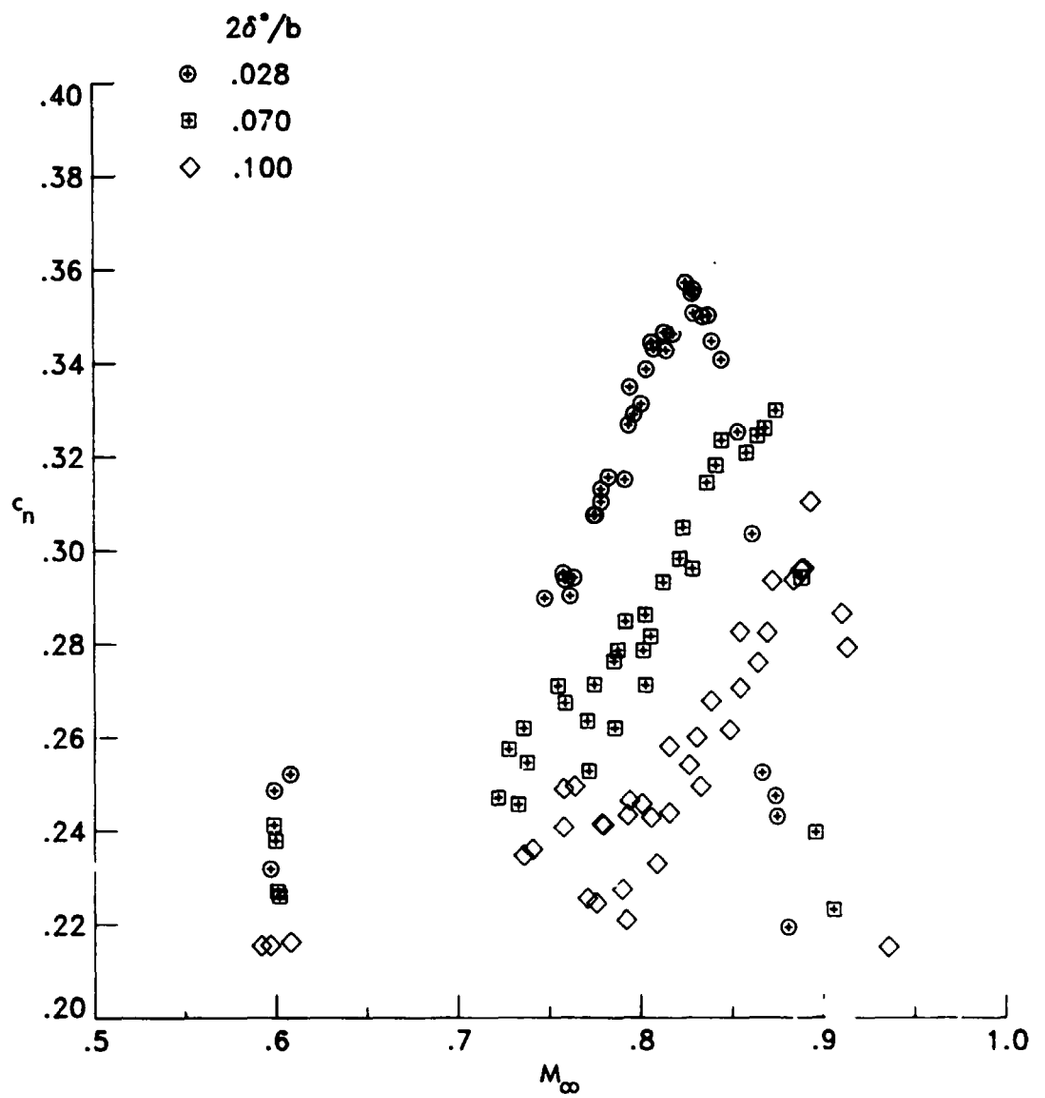

(a) Normal-force coefficient vs. measured freestream Mach number.

Figure 22.- Variation of normal-force coefficient with freestream Mach number for the NLR-1 airfoil tested with three sidewall boundary-layer displacement thicknesses. Angle of attack is 2.0 degrees.

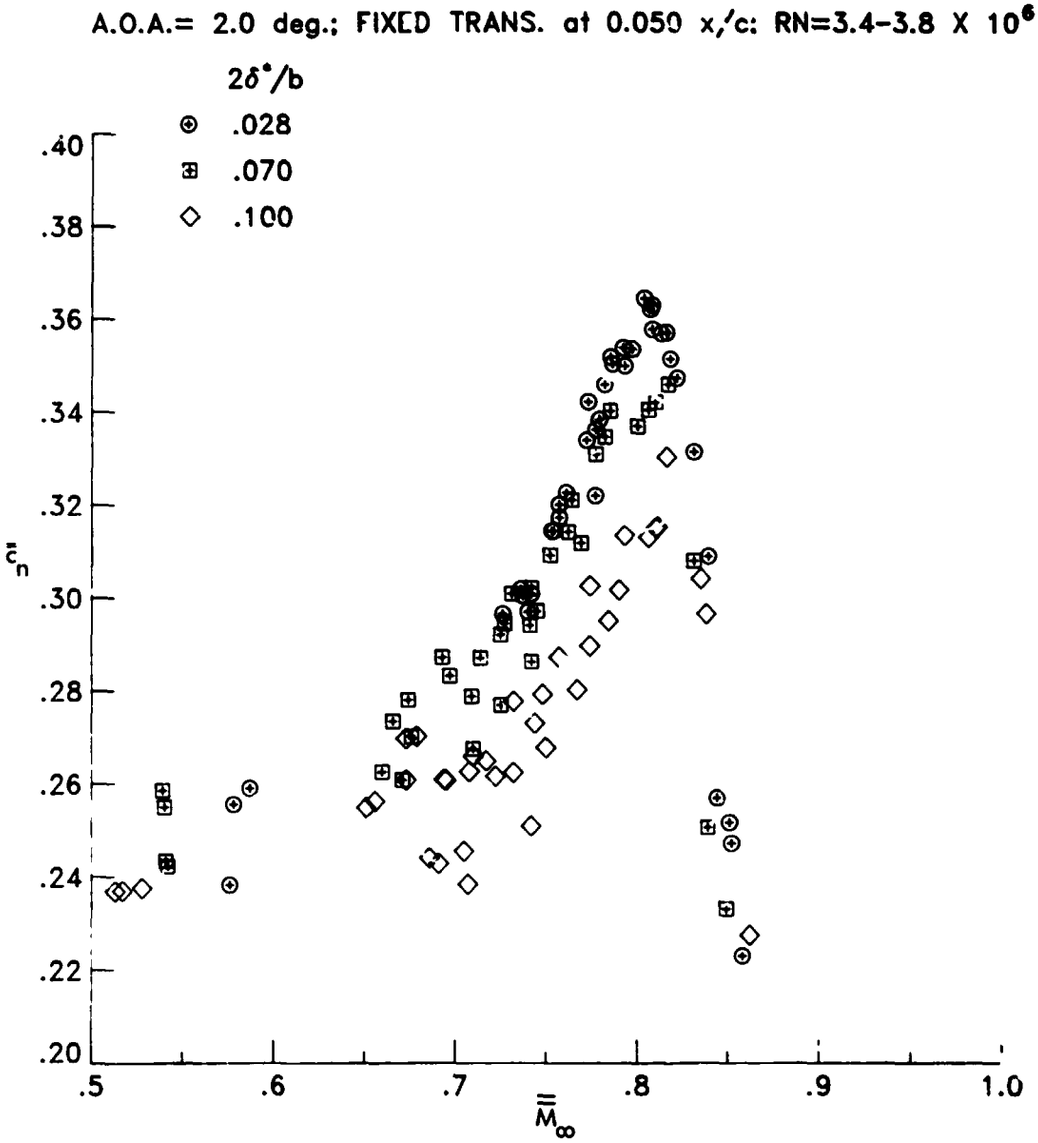

(b) Adjusted normal-force coefficient vs. equivalent freestream Mach number.

Figure 22.- Concluded.

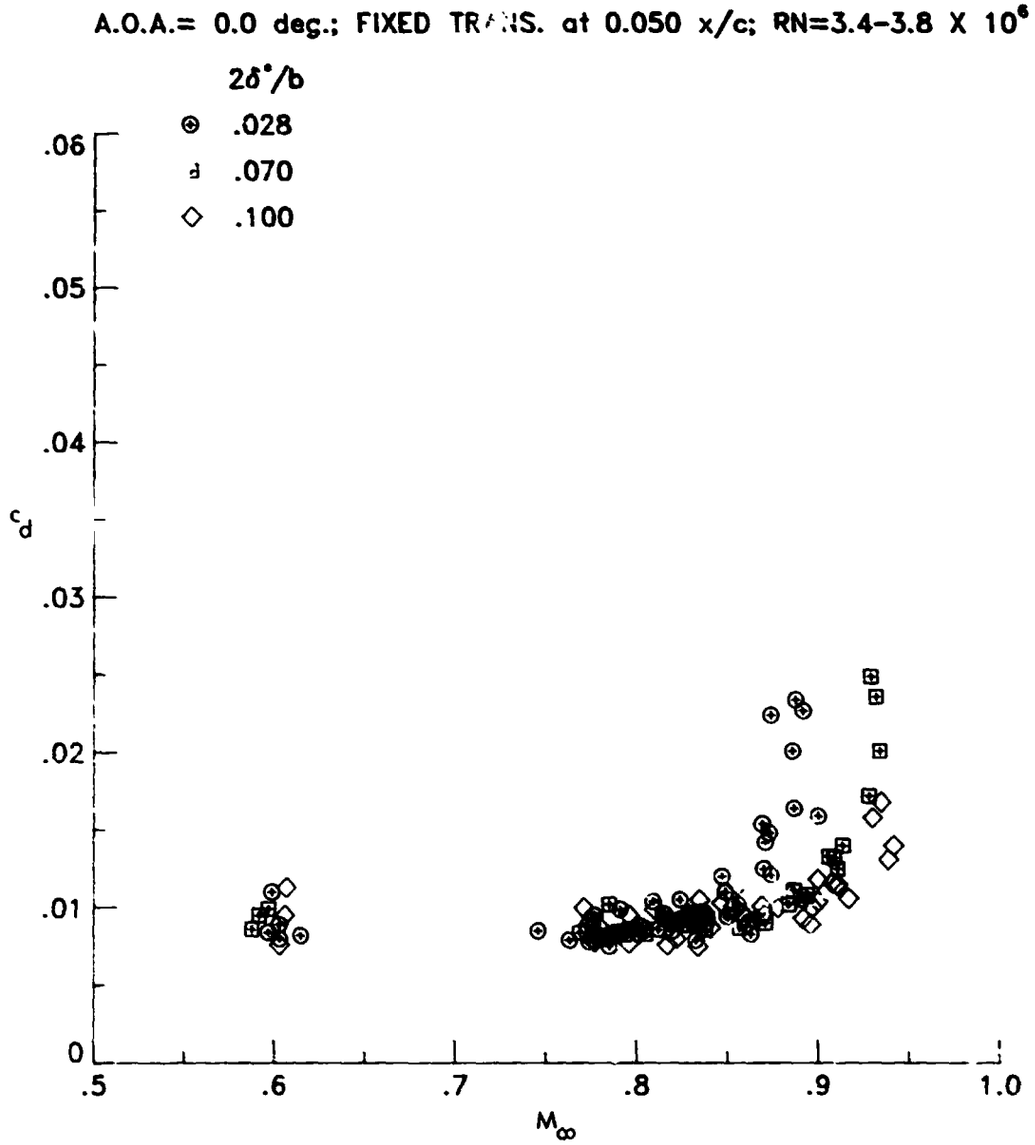

(a) Section drag coefficient vs. measured freestream Mach number.

Figure 23.- Variation of section drag coefficient with freestream Mach number for the NLR-1 airfoil tested with three sidewall boundary-layer displacement thicknesses. Angle of attack is 0 degrees.

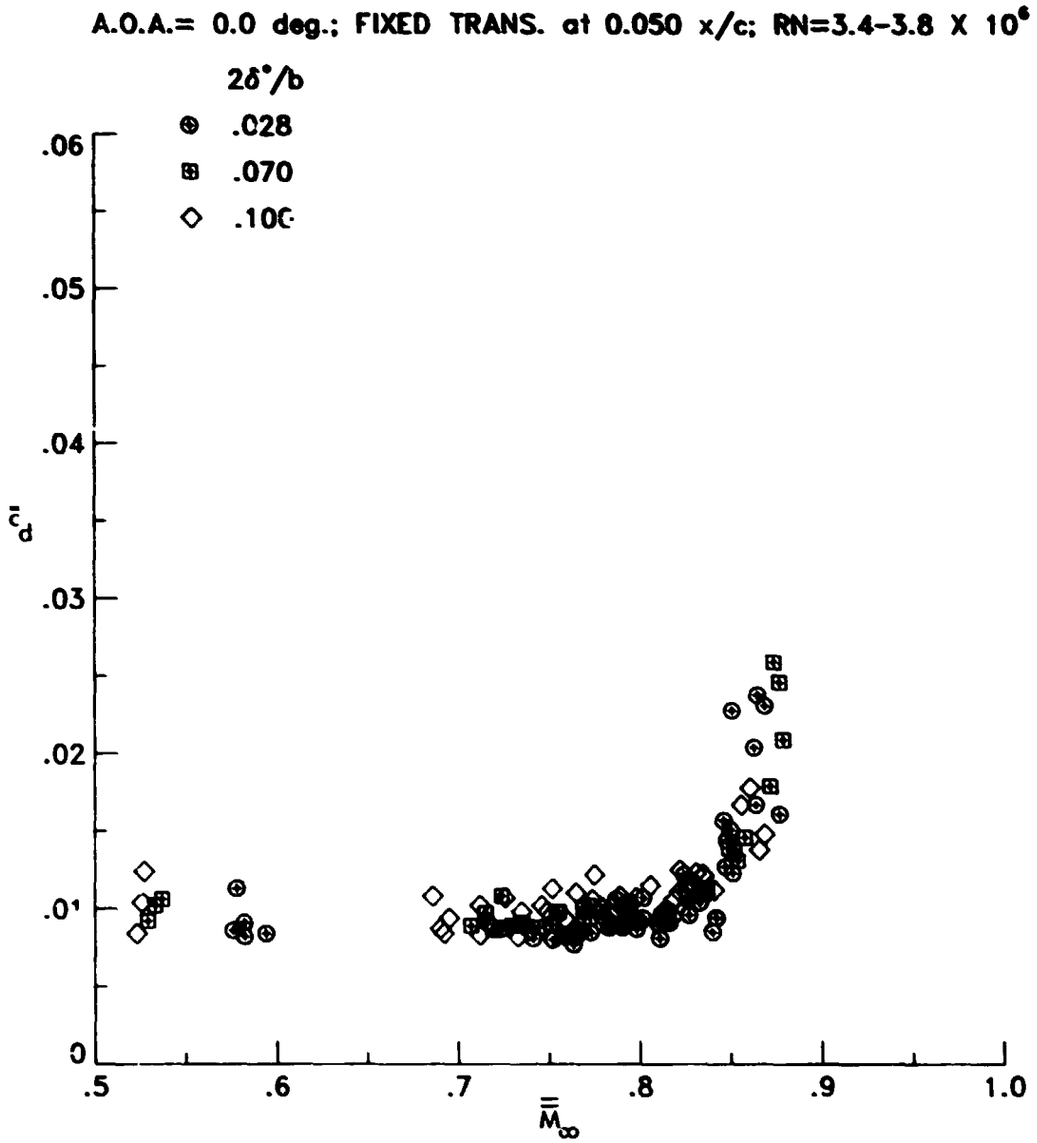

(b) Adjusted section drag coefficient vs. equivalent freestream Mach number.

Figure 23.- Concluded.

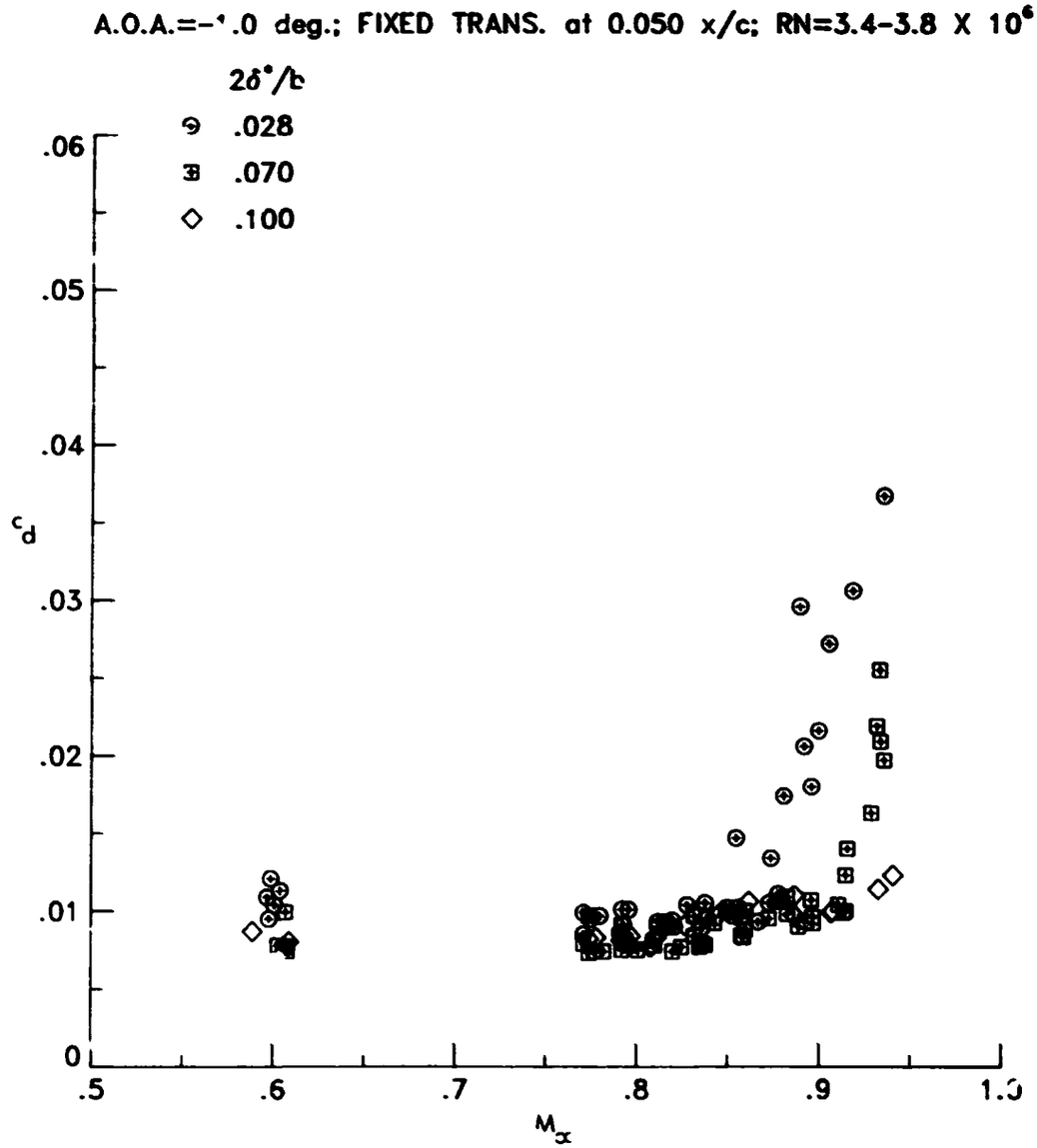

(a) Section drag coefficient vs. measured freestream Mach number.

Figure [illegible] Variation of section drag coefficient with freestream Mach number for the NLR-1 airfoil tested with three sidewall boundary-layer displacement thicknesses. Angle of attack is -1.0 degree.

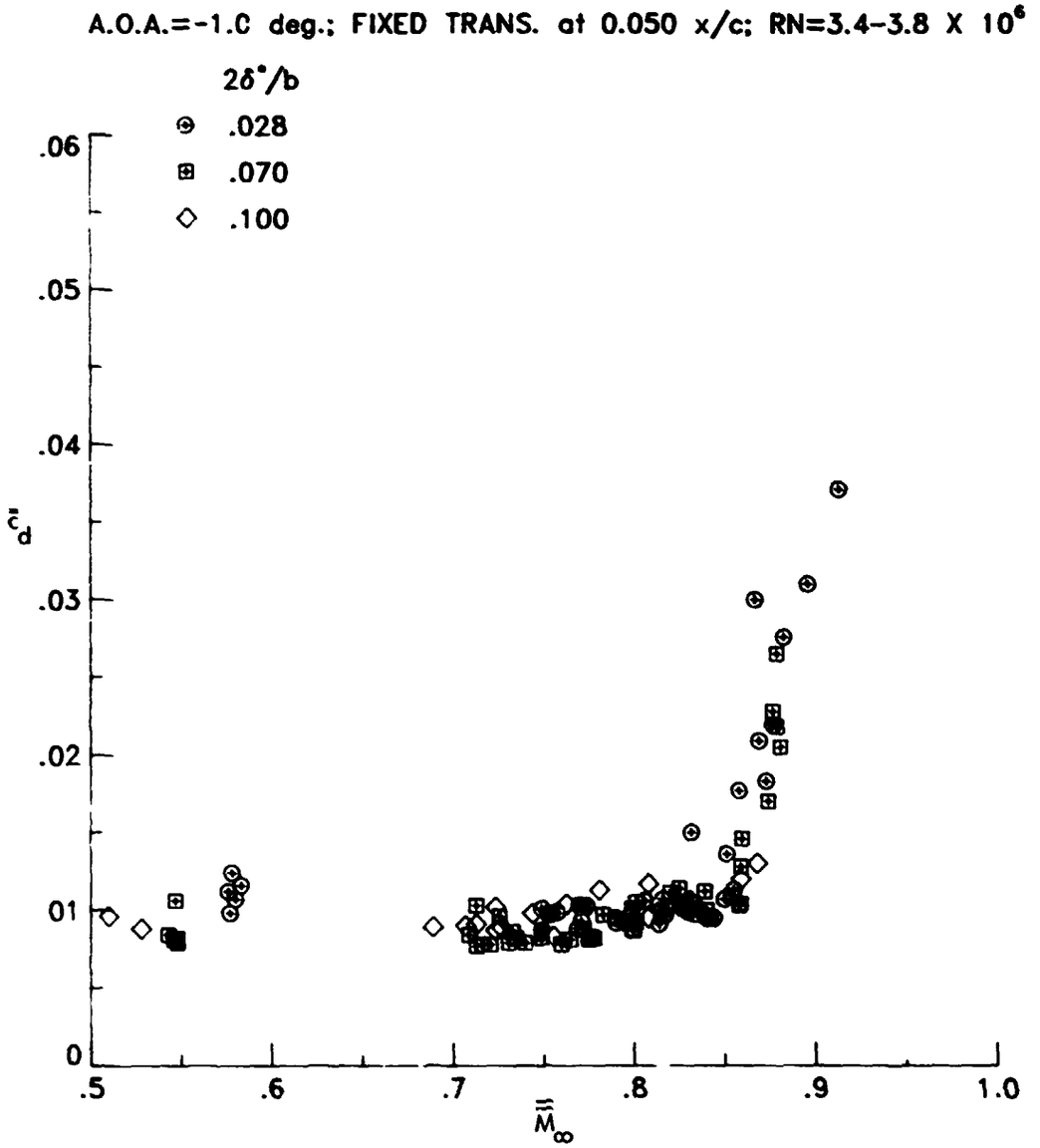

(b) Adjusted section drag coefficient vs. equivalent freestream Mach number.

Figure 24.- Concluded.

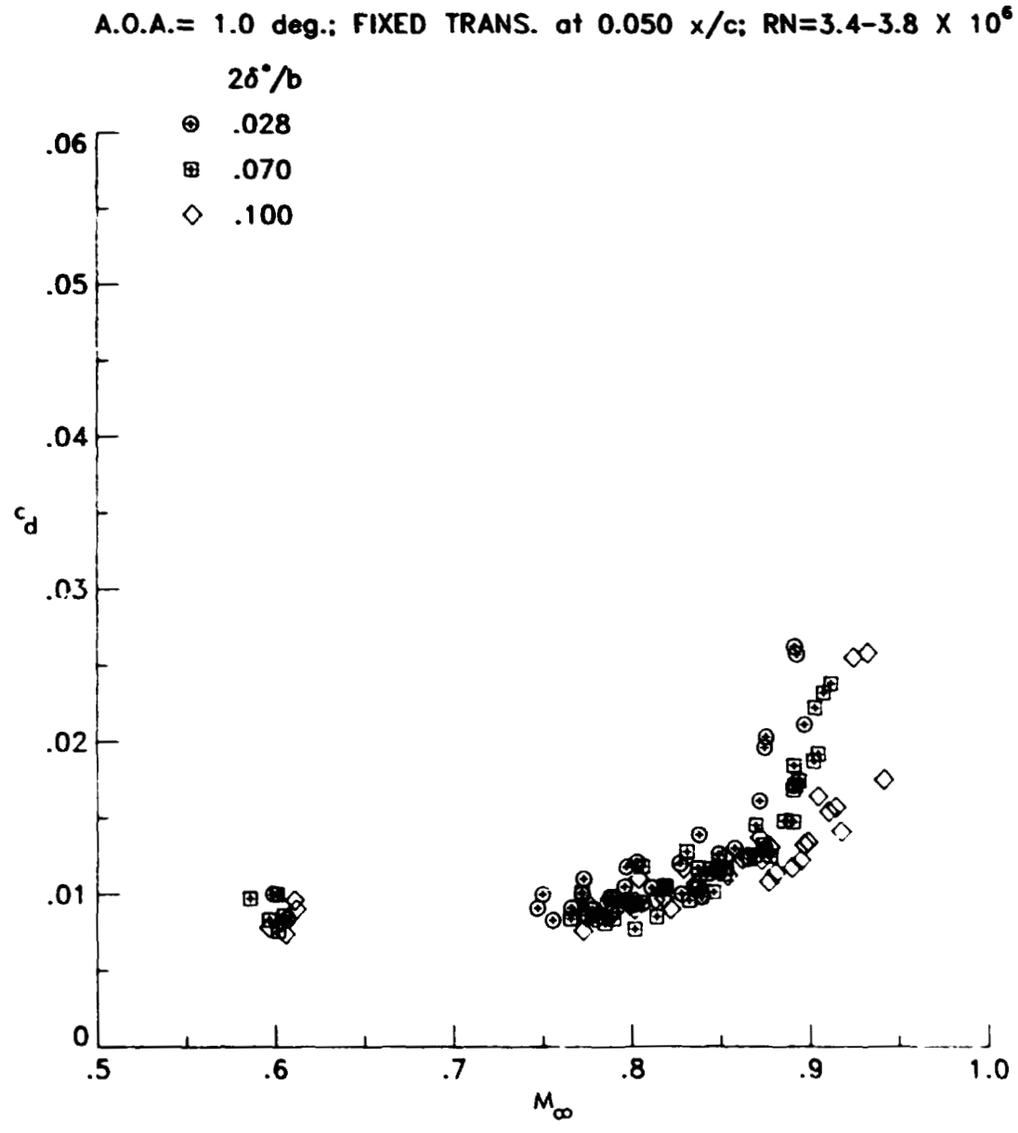

(a) Section drag coefficient vs. measured freestream Mach number.

Figure 25.- Variation of section drag coefficient with freestream Mach number for the NLR-1 airfoil tested with three sidewall boundary-layer displacement thicknesses. Angle of attack is 1.0 degree.

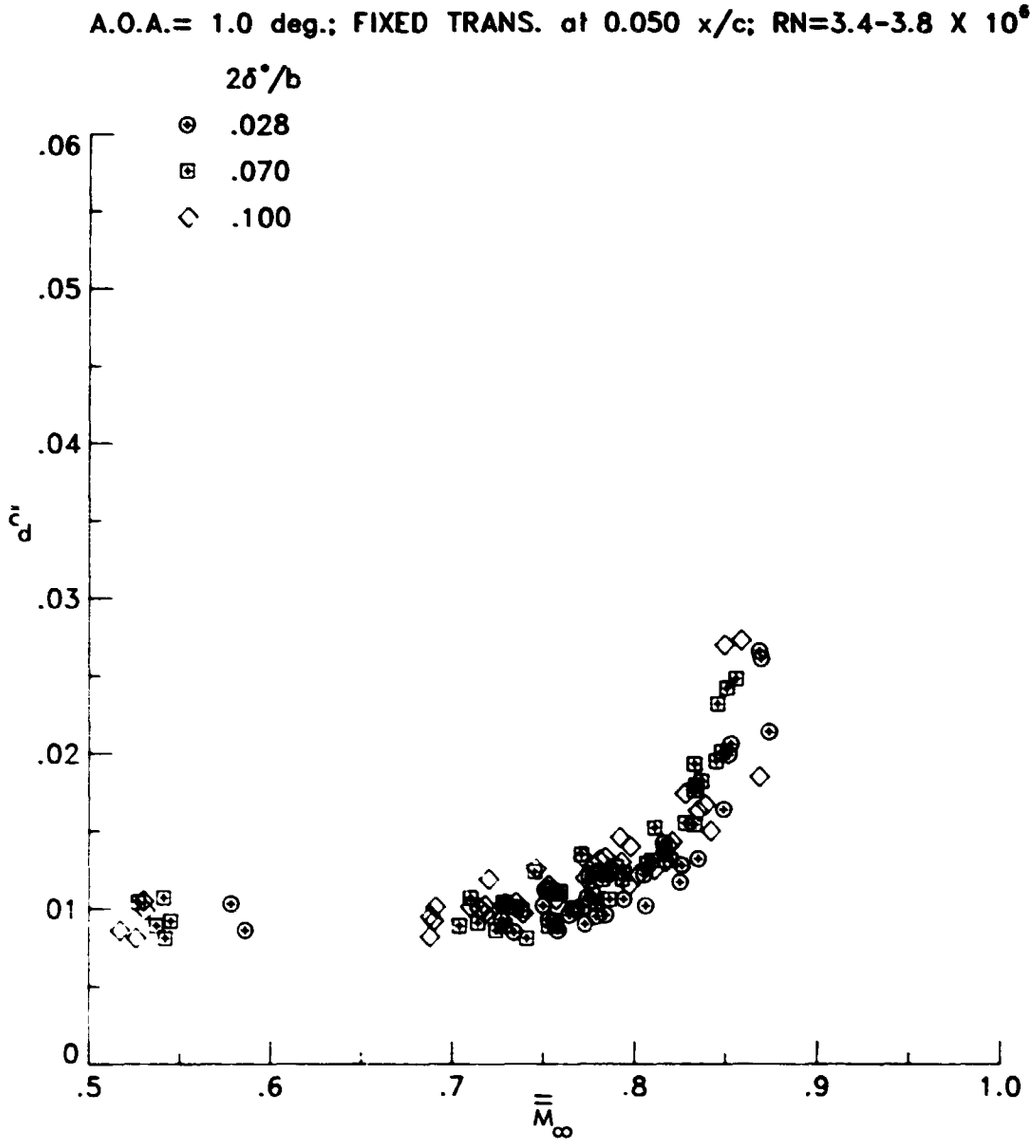

(b) Adjusted section drag coefficient vs. equivalent freestream Mach number.

Figure 25.- Concluded.

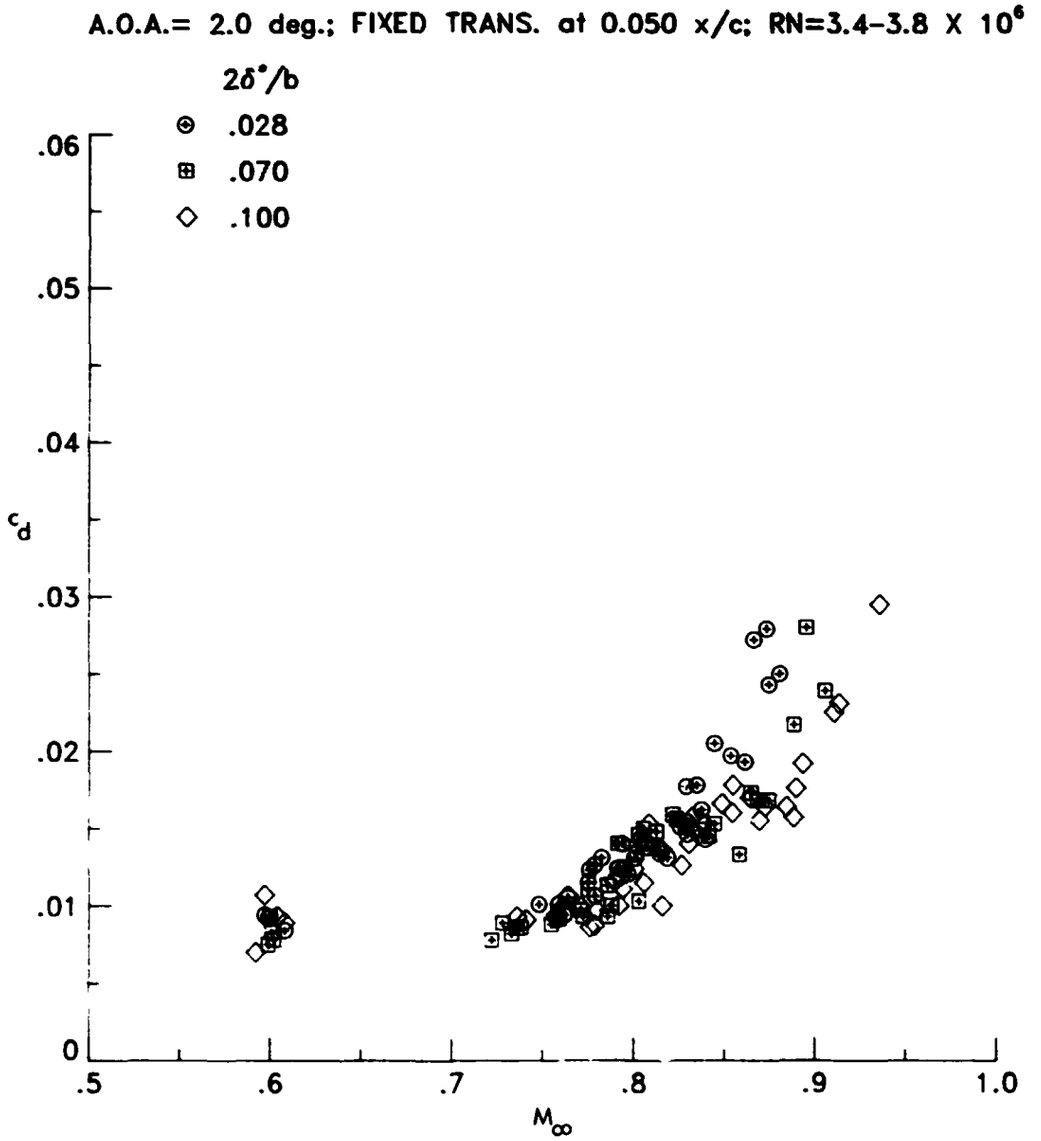

(a) Section drag coefficient vs. measured freestream Mach number.

Figure 26.- Variation of section drag coefficient with freestream Mach number for the NLR-1 airfoil tested with three sidewall boundary-layer displacement thicknesses. Angle of attack is .0 degrees.

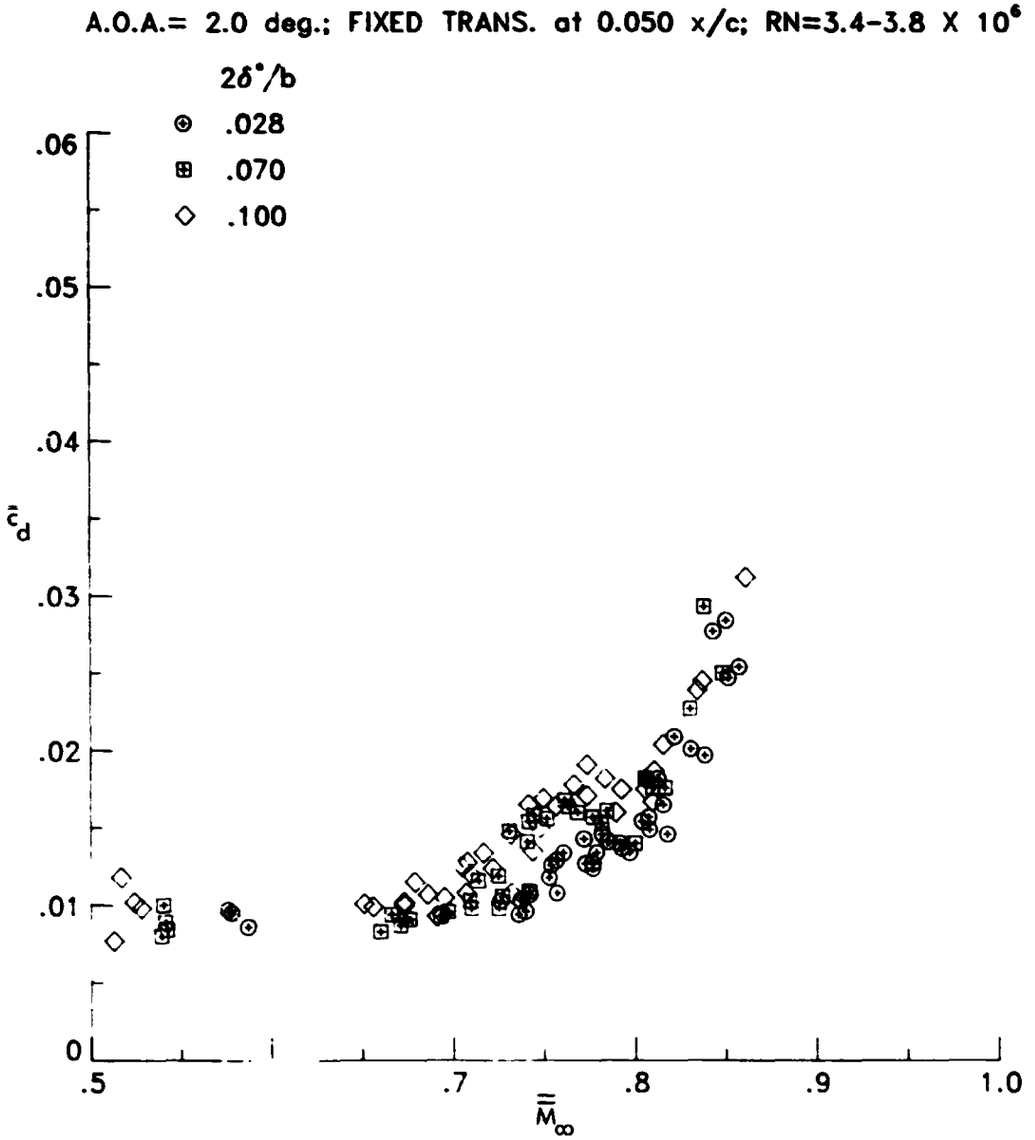

(b) Adjusted section drag coefficient vs. equivalent freestream Mach number.

Figure 26.- Concluded.